

THE BEHAVIOR OF TELLURIUM DURING COPPER ORE PROCESSING AT THE AMERICAN  
SMELTING AND REFINING COMPANY (TUCSON, AZ)

By

Amy E. Josephson

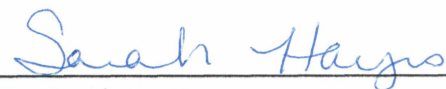
RECOMMENDED:



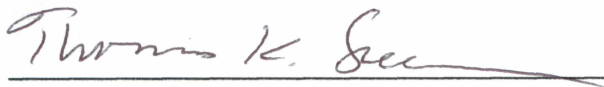
Dr. Rainer J. Newberry



Dr. Thomas P. Trainor



Dr. Sarah M. Hayes  
Advisory Committee Chair

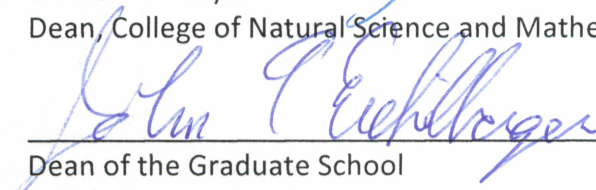


Dr. Thomas K. Green  
Chair, Department of Chemistry and Biochemistry

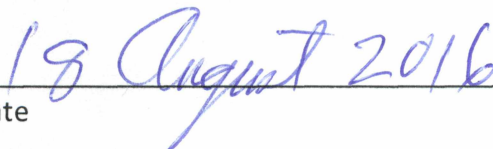
APPROVED:



Dr. Paul W. Layer  
Dean, College of Natural Science and Mathematics



Dean of the Graduate School



Date



THE BEHAVIOR OF TELLURIUM DURING COPPER ORE PROCESSING AT THE AMERICAN  
SMELTING AND REFINING COMPANY (TUCSON, AZ)

By

Amy E. Josephson, B.S.

A Thesis Submitted in Partial Fulfillment of the Requirements  
for the Degree of

Master of Science

in

Environmental Chemistry

University of Alaska Fairbanks

August 2016

APPROVED:

Sarah M. Hayes, Committee Chair

Rainer J. Newberry, Committee Member

Thomas P. Trainor, Committee Member

Thomas K. Green, Chair

*Department of Chemistry and*

*Biochemistry*

Paul W. Layer, Dean

*College of Natural Science and*

*Mathematics*

Michael A. Castellini, *Dean of the Graduate*

*School*

## Abstract

Essentially all tellurium (Te), an element used in solar panels and other high technology devices, is recovered as a byproduct of copper mining. Recent increases in demand have sparked questions of long-term supplies of Te (crustal abundance  $\sim 3 \mu\text{g}\cdot\text{kg}^{-1}$ ). As part of a larger study investigating Te resources, this project examines the behavior of Te during Cu ore mining, smelting, and refining at the American Smelting and Refining Company (Tucson, AZ) as a first step toward optimizing Te recovery. Mass balance calculations estimate that only  $4 \pm 1\%$  of the Te in the ore reports to the Cu anodes, while  $60 \pm 30\%$ ,  $0.8 \pm 0.2\%$  and  $5.8 \pm 0.4\%$  is lost in the tailings, slag, and dust, respectively. The uncertainties reported are the standard deviation of analytical measurements, but due to heterogeneity of Te distribution in the ore, the actual uncertainty is likely higher. Microprobe data shows that Te in the concentrate is mainly present as telluride minerals, but substitution into sulfides most likely also occurs. X-ray fluorescence (XRF) mapping showed that Te is collocated with S in the raw anode slimes, pressed anode slimes, and doré furnace soda slag. X-ray absorption spectroscopy (XAS) was used to examine Te speciation in anode slimes. It was found that Te oxidizes during the Cu ore smelting process, with 44%  $\text{Te}^{4+}$  in the flash furnace  $\text{SO}_2$  filter. Te also showed 32%  $\text{Te}^{4+}$  in the raw and pressed anode slimes. The doré furnace soda slag and dust filter showed the most oxidation of Te at 57%  $\text{Te}^{4+}$  and 60%  $\text{Te}^{6+}$  respectively. These results indicate several points in the extraction process that could be examined further to determine if additional Te might be recovered from the overall process.



## Table of Contents

	Page
Title Page.....	i
Abstract.....	iii
Table of Contents.....	v
List of Figures .....	ix
List of Tables .....	xi
Acknowledgements.....	xii
Chapter 1 Introduction .....	1
1.1 What is Tellurium?.....	1
1.2 Tellurium End Uses and Market.....	1
1.3 Global Supply of Tellurium.....	5
1.4 Tellurium Scarcity and Criticality .....	7
1.5 Current Copper Extraction Process.....	9
1.5.1 Copper Mining .....	10
1.5.2 Copper Smelting .....	11
1.5.3 Copper Refining .....	12
1.6 Tellurium Byproduct Recovery .....	13
1.6.1 Mineralogy of Tellurium in Ore Deposits.....	13
1.6.2 Behavior of Tellurium during Copper Concentration .....	15
1.6.3 Behavior and Mineralogy of Tellurium in Copper Anodes and Anode Slimes ..	16
1.6.4 Extraction of Tellurium as a Copper Byproduct.....	17
1.7 Research Objectives.....	19
Chapter 2 Site Description .....	21
2.1 The Mines.....	21
2.2 The Smelter .....	21
2.3 The Refinery .....	22
Chapter 3 Methods.....	23
3.1 Sample and Standard Collection, Preparation, and Preservation .....	23

3.2 Elemental Analysis .....	25
3.2.1 Inductively Coupled Plasma Mass Spectrometry .....	25
3.2.1.1 Method Development of Sodium Peroxide Sinter .....	27
3.2.1.2 Sample Preparation for ICP-MS .....	28
3.2.1.3 ICP-MS Elemental Analysis .....	29
3.2.2 Wavelength Dispersive X-Ray Fluorescence .....	30
3.2.2.1 Sample Preparation and Analysis of WD-XRF .....	31
3.3 Mass Balance Calculations .....	32
3.4 X-Ray Absorption Spectroscopy .....	32
3.4.1 Bulk S XAS .....	34
3.4.1.1 Bulk S XAS Collection .....	34
3.4.1.2 S XAS Data Analysis .....	35
3.4.1.3 S Linear Combination Fitting .....	36
3.4.2 Bulk Te XAS .....	37
3.4.2.1 Bulk Te XAS Collection .....	38
3.4.2.2 Te XAS Data Analysis .....	38
3.4.2.3 Te Linear Combination Fitting .....	39
3.5 Microfocused X-Ray Fluorescence Map Collection and Analysis .....	39
3.5.1 Experimental Conditions .....	40
3.5.2 Map Analysis .....	41
3.6 Electron Microprobe Analysis .....	43
3.6.1 Experimental Conditions .....	45
Chapter 4 Results .....	47
4.1 Method Development and Verification .....	47
4.2 Elemental Analysis of Samples .....	48
4.3 Mass Balance .....	50
4.4 X-Ray Absorption Spectroscopy .....	53
4.4.1 Sulfur .....	53
4.4.2 Tellurium .....	55

4.5 Micro-focused X-Ray Maps .....	59
4.6 Electron Microprobe Analysis .....	60
Chapter 5 Discussion .....	63
5.1 Mass Balance .....	63
5.2 Mine .....	65
5.3 Smelter .....	65
5.4 Refinery .....	66
Chapter 6 Conclusions .....	69
6.1 Future Directions .....	70
References .....	71





## List of Figures

	Page
Figure 1.1 End-uses of Te from 1917 to 2010.....	2
Figure 1.2 The price of Te from 1917 to 2014 in dollars per kg .....	4
Figure 1.3 First Solar sales from 2006 to 2014 .....	5
Figure 1.4 Approximate world's production of Te and Cu from 1930 to 2003 .....	7
Figure 1.5 Percentage of Cu produced by SX-EX .....	7
Figure 1.6 Simple systemic of the Cu mining, smelting and refining process .....	10
Figure 1.7 The electrochemical dissolution of Cu anodes .....	12
Figure 1.8 Mass balance of Te for a Russian Cu mine and smelter in the 1970s .....	13
Figure 1.9 Eh-pH diagram of Te aqueous speciation .....	15
Figure 1.10 Backscattered electron microscope image of a Cu anode slime .....	17
Figure 1.11 Processing of Te from raw anode slimes to pure Te metal .....	18
Figure 1.12 Recovery of Te from leach after autoclave decopperization .....	19
Figure 2.1 The ASARCO Hayden Smelter diagram .....	22
Figure 3.1 Sample path for ICP-MS analysis .....	26
Figure 3.2 Path of x-rays during WD-XRF analysis .....	31
Figure 3.3 Possible energy transitions elements can undergo .....	34
Figure 3.4 XAS spectra for reduced and partially oxidized sulfur reference samples .....	37
Figure 3.5 XAS spectra for fully oxidized sulfur reference samples .....	37
Figure 3.6 XAS spectra for Te reference samples used for LCF .....	39
Figure 3.7 Te counts vs Ca counts in Te and Ca XRF standards .....	42
Figure 3.8 Instrument schematic of a typical microprobe.....	44
Figure 4.1 Mass balance of Te during the mining and smelting process .....	52
Figure 4.2 S XAS spectra of furnace dust (sample 351) and converter dust (sample 353) .....	54
Figure 4.3 S XAS spectra of the raw anode slimes (sample 354) and the pressed anode slimes. ....	55
Figure 4.4 Te XAS spectra of the flash furnace dust (sample 351) .....	56
Figure 4.5 Te XAS spectra of the raw anode slimes (sample 354) and the pressed anode.....	57
Figure 4.6 X-ray fluorescence maps showing the correlation between Te and S .....	60

Figure 4.7 Backscattered electron images of Cu concentrate samples..... 61  
Figure 4.8 Backscattered electron images of the raw slimes ..... 62

## List of Tables

	Page
Table 1.1 Examples of some Te bearing minerals .....	14
Table 3.1 List of ASARCO sample numbers, description, location, and date collected .....	23
Table 3.2 Sources of S and Te reference compounds.....	24
Table 3.3 Background removal parameters for S XAS analysis .....	35
Table 3.4 Background removal parameters for Te XAS analysis .....	38
Table 3.5 Energy windows used to examine Te.....	41
Table 3.6 Emission energies for elements with potential interferences with Te overlap.....	41
Table 4.1 NIST 2780 standard reference material analysis .....	47
Table 4.2 CCU-1d standard reference material analysis .....	48
Table 4.3 Inductively coupled plasma mass spectrometry results.....	49
Table 4.4 X-ray fluorescence results.....	51
Table 4.5 Linear combination fits for S XAS.....	55
Table 4.6 Linear combination fits results for Te XAS .....	58
Table 4.7 The composition by weight percent of Te-bearing grains in concentrate.....	61
Table 4.8 The composition by weight percent of Te-bearing grains found in anode slimes .....	62



## **Acknowledgements**

This thesis would not have been possible without guidance and support of Dr. Sarah Hayes, my academic advisor, and Drs. Rainer Newberry and Thomas Trainor, my committee members. A special thank you goes to Drs. Newberry and Severin for teaching me the feature sizing program on the microprobe and to Karen Spaleta for helping me develop the sodium peroxide sinter method to analyze my samples. I deeply appreciate the support and encouragement I received from the Hayes, Trainor, and Guerard lab groups. Furthermore, this project could not have been completed without funding from USGS Mineral Resources External Research Program.



## Chapter 1 Introduction

### 1.1 What is Tellurium?

Tellurium (Te) is a rare metalloid and semi-conductor, with an average crustal abundance of  $3 \mu\text{g}\cdot\text{kg}^{-1}$  [1]. Tellurium has an atomic number of 52 and an atomic mass of  $127.6 \text{ g}\cdot\text{mol}^{-1}$  and occurs in group 16, underneath sulfur (S) and selenium (Se), of the periodic table. Because of this, it is often assumed that Te will behave similarly to S and Se in the natural environment [2], but recent literature has challenged this assumption [3]. Like S, Te has four naturally occurring oxidation states: native Te ( $\text{Te}^0$ ), telluride ( $\text{Te}^{0\geq 2-}$ ), tellurite ( $\text{Te}^{4+}$ ), and tellurate ( $\text{Te}^{6+}$ ).

Tellurium was first discovered in 1782 by Baron Franz Joseph Müller von Reichenstein. Müller discovered the element when he extracted it from a bluish-white ore of gold. At first he believed the metal to be antimony (Sb), but upon further examination decided that it was not Sb and, therefore, must be a new element. His discovery was mostly forgotten until Martin Heinrich Klaproth read Müller's paper on the gold ore to the Academy of Sciences in Berlin in 1798. At this meeting it was decided to name the element tellurium, meaning earth [4].

As the industrial importance of Te increases, there is a need for improved understanding of the effects of Te on organisms and the environment. Compounds that exhibit greater solubility tend to demonstrate greater toxicity [5]. Soluble Te is highly toxic to most microorganisms and is also considered toxic to humans [6]. Tellurite is reported to be slightly more toxic than selenite and arsenite, and ten times more toxic than tellurate. The main target sites for human toxicity are the nervous system, kidneys, skin, and fetus. The symptoms of tellurium exposure is often characterized by a garlic like smell on the breath that is caused by the formation of  $(\text{CH}_3)_2\text{Te}$  [5]. While, there are concerns about Te toxicity, acute poisoning is rare, and presently, Te is not considered to be carcinogenic [6].

### 1.2 Tellurium End Uses and Market

Tellurium has been used for industrial purposes since 1917, when it was first used in the production of rubber (**Figure 1.1**). Tellurium, when added to rubber and elastomers in either its



elemental form or as ethyl telluric (diethyldithiocarbamate, TDEC), aids in the curing process [7]. While it was in rubber that Te was first used, this application no longer dominates the market. In fact, this end-use accounts for less than 5% of the total Te consumed today [8].

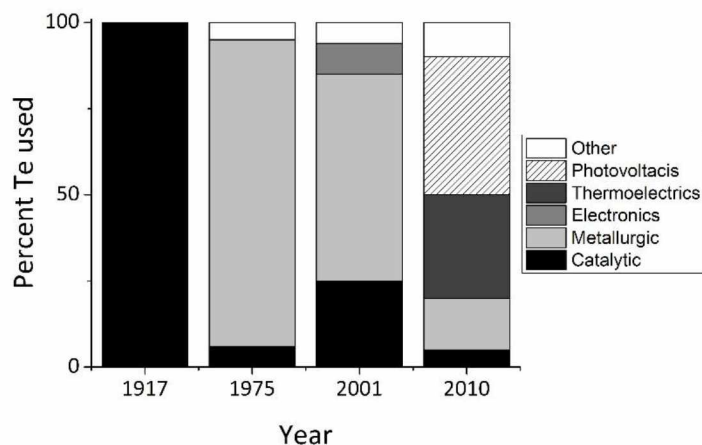


**Figure 1.1** End-uses of Te from 1917 to 2010. It is important to note that the 9% electronic end use in 2001 grew to 70% (30% thermoelectric, 40% photovoltaic) in 2010 [8-10].

Another end use for Te today is in metallurgy, where Te is used as an alloying agent with iron, steel, and other metals to improve machining characteristics [7]. Tellurium is often included in low-carbon steels, resulfurized steels, and leaded steels. In lead alloys (Pb, 0.05% Te, 0.06% Cu) the addition of small mass fractions of Te can result in higher fatigue strength and increases in recrystallization temperatures. This allows for lead alloys to be used in sheathing communication and power cables, particularly in corrosive marine environments. This alloy is also used as a reactor shield and for the containment of hot wastewater in the nuclear industry. Tellurium can also be used in copper alloys where it greatly improves the machinability of the copper with only minimal decreases in its thermal and electrical conductivity [7]. As recently as the early 2000's this was primary industrial use of Te, but metallurgy currently accounts for only 15% of the Te consumed [8].

As a metalloid, Te exhibits both metal and non-metal properties, making it a natural semiconductor. At room temperature, Te has a thermal energy gap of 0.32 to 0.38 eV. One of Te's unique properties is that its energy gap temperature coefficient is positive, which differs

from majority of semi-conductors which have a negative energy gap [11]. This allows for Te to be a p-type semiconductor [12], and makes Te an unparalleled material in the fields of thermoelectrics and photovoltaics.

Approximately one-third of Te consumed in 2010 was used in the production of thermoelectric materials such as bismuth telluride ( $\text{Bi}_2\text{Te}_3$ ) [13]. Thermoelectric-based devices use differences in temperature to produce electricity. The use of Te in thermoelectric devices is based off the physics of the Peltier effect, Seebeck effect, and Thompson effect which all help define the relationship between electromotive force and temperature gradient between two dissimilar metals. These thermoelectric are used as coolers in devices where temperature stabilization is critical, including lasers, thermal detectors [7], and medical instruments [1]. A small fraction of refrigerators and microrefrigerators also use Te bearing semiconductors.

Currently, the number one end-use of Te is in photovoltaic (PV) cells, accounting for 40% of industrial Te consumption in 2010 [13]. Tellurium is a major component of thin-film CdTe PV cells. Cadmium-Telluride PV cells are more than 50% Te by weight and must be synthesized with the use of high-purity grade Te [7]. Tellurium application in the semiconducting layer of solar cells can produce some of the highest power conversions seen in solar cells to date [7]. The energy payback time (EPBT) for CdTe solar cells is estimated to be 1.0 to 1.1 years. This is much less than that of traditional silicon based solar cells, which range from 1.5 to 2.5 years and can be as high as 4.4 years in some environments [14]. Recent growth in this industry has stressed the current supply of Te and created uncertainty about feasibility of large-scale CdTe PV deployment [15].

Historic changes in the end-uses of Te, shown in **Figure 1.1**, have been accompanied by historic price volatility. Since the mid 1970's the market price of Te has significantly increased, sometimes with dramatic fluctuations, especially during the past 15 years [1]. During this period, the price of Te ranged as low as \$32.9/kg in 2003 to as high as \$349/kg in 2011. Since 2011, the price of Te has dropped dramatically and sold for \$112/kg in 2013 and increased slightly to \$117/kg in 2014 (**Figure 1.2**) [16, 17].

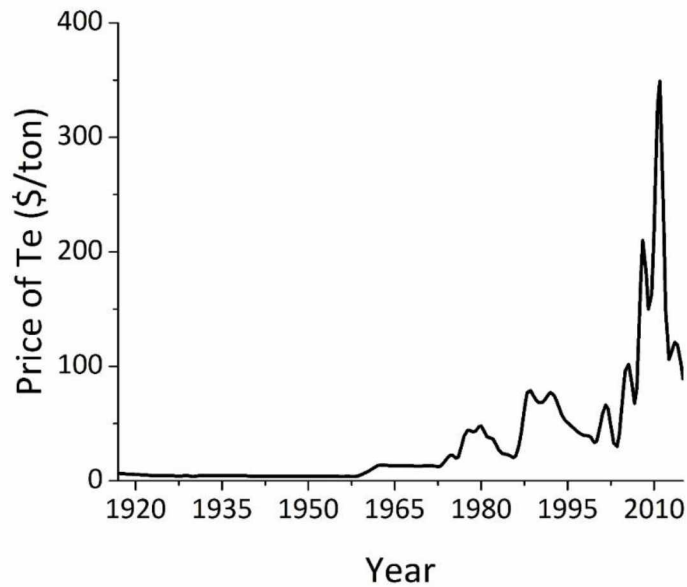


**Figure 1.2** The price of Te from 1917 to 2014 in dollars per kg. As the graph depicts, since 1975, the market price of Te has experienced substantial volatility [8].

One possible explanation for the historic fluctuations in Te prices is the increase in demand for Te from the manufacturers of CdTe PV cells, coupled with the increase in demand from China where Te is needed for metallurgy [18]. First Solar, the main producer of CdTe PV's [1] was founded in 1999, and began sales in 2002. By 2005, they had installed enough CdTe PV's to produce 25 MW. Since 2005 their sales have dramatically increased, with over 10 GW of electricity produced by First Solar panels worldwide. In 2006 they sold \$13.5 million worth of CdTe PV's. However, since 2012 they have been averaging ~\$3.3 billion in sales (**Figure 1.3**) [19].

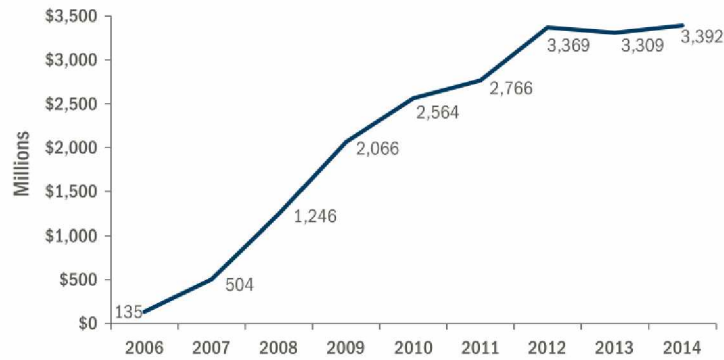


**Figure 1.3** First Solar sales from 2006 to 2014 [19]

Another factor potentially contributing to market volatility is the lack of transparency in the Te market, due to minimal truly open markets for Te. The majority of Te is sold through long-term supply contracts, which allows the speculative bubbles in Te price such as those seen in 2008 and 2011. Speculative price bubbles are caused by a perceived supply limit, which causes many consumers to stock up on Te. After it has been realized that there was not a true supply limit, the market adjusts, leading to a rapid decrease in the price. The price volatility of Te poses a significant threat to both the producers and consumers of Te. It effects the producers because they are unsure if it will continue to be profitable to produce Te, and it effects the consumers because they cannot afford to manufacture their products if the price become too high [20].

### *1.3 Global Supply of Tellurium*

There are three main potential sources for Te production: (1) gold, silver telluride deposits, (2) the direct mining of Te, and (3) copper ore deposits. Most of the Te present in the earth's crust occurs as telluride minerals associated with precious-metal-bearing deposits. However, these deposits are not a significant source of commercially available Te, in part, because the modern processes used for gold and silver extraction do not allow for the recovery Te [1].

One of the reasons the direct mining of Te is not widely practiced is that the concentration of Te would have to be significantly greater than  $200 \text{ mg}\cdot\text{kg}^{-1}$  for the mining

operation to be profitable, such concentrations in large volumes of rock have only been reported at a few locations and most of these are currently mined for gold [21]. There are three locations where Te is mined as the primary product—the Dashuigou and Majiagou epithermal deposit located in southwestern China, the Kankberg volcanogenic massive sulfide deposits in Sweden [1], and Moctezuma mining district in Mexico [22]. The direct mining of Te only accounts for 10-15% of the global production of Te [1].

Nearly all Te on the market today is a byproduct of copper (Cu) ore smelting (~75%) and to a lesser extent iron (Fe) ore smelting (~10%) [8]. This has made the production of Te more dependent on Cu demand and production rather than the demand of Te. This relationship is further complicated by the fact that Te can only be extracted from the anode slimes of copper ore that have been recovered by pyrometallurgical processes (also known as electrorefining), which is typically only applied to high grade copper sulfide ores [1]. Approximately two-third of the world's Cu production is recovered by pyrometallurgy [23]; however, this percentage is expected to continue to decrease as technological advances are made in solvent extraction electrowinning (SX-EW) [24]. The increase use of SX-EW of Cu raises concerns about the ability of the Cu market to continue to produce the world's needed Te [25].

Tellurium production has historically been volatile. This is due in part to the byproduct extraction tying Te production to the demand and production of Cu rather than the demand for Te. However, careful examination of the correlation between the production of Cu and Te over the years shows that the production of Te does not always have a direct correlation to that of Cu (**Figure 1.4**). From about 1930 to 1980 an increased Cu production led to an increase in the production of Te, but after 1980, Cu production continued to increase while Te's production decreased. This could be in part because the demand for Te decreased in the late 1980's due to the decreased need for Te in metallurgy [26]. Another possible explanation for the increase in Cu production without a noticeable increase in Te production is the steady increase of the production of Cu by SX-EW (**Figure 1.5**) [24].

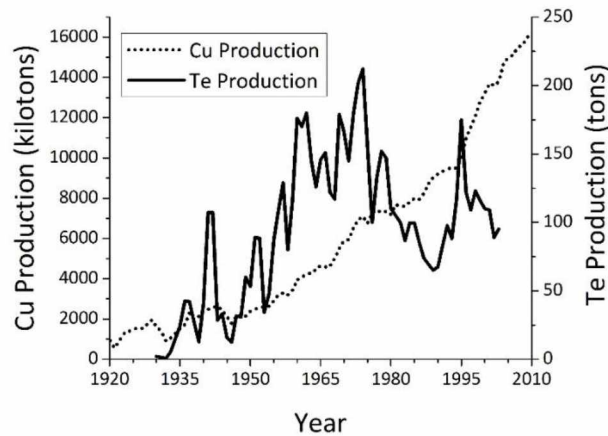


**Figure 1.4** Approximate world's production of Te and Cu from 1930 to 2003. Although the production of Te and Cu can be closely tied, more recent years do not show a direct correlation between the production of Te and Cu. Data for production since 2003 has been withheld by the USGS to avoid publishing propriety data [16, 17].

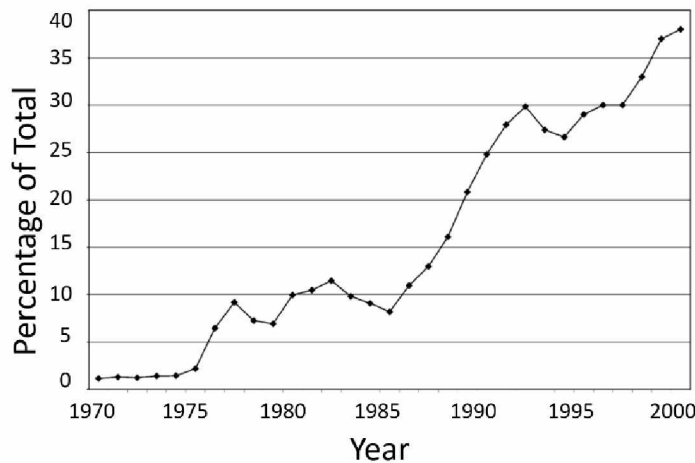


**Figure 1.5** Percentage of Cu produced by SX-EX. Since the mid 1980's there has been a steady increase in the percentage of Cu produced by SX-EX [24].

#### 1.4 Tellurium Scarcity and Criticality

The global production of PVs has grown from 0.202 GW in 1999 [15] to 68 GW in 2011 [22], demonstrating the growth in demand for high efficiency PV cells, a promising alternative energy source [14]. Photovoltaics currently supply only 0.1% of the world's electricity; however, it is estimated that this will grow to 2.5-25% by 2050, depending on the model used [14]. Thin-film PV cells, such as CdTe PV cells, are predicted to play a major role in the growth

of solar energy production [18]. In 2009, CdTe PV cell accounted for about ten percent of PV sold, and this is expected to grow to 20-25% by 2020 [14]. Cadmium-telluride PVs are of interest in implementation of PVs as an energy source because they are currently the cheapest to produce, costing \$0.74/watt peak (Wp). However, the concern about long-term supply and price volatility of Te presents a significant potential barrier for the production and continued implementation of CdTe PV cells [18].

It is estimated that it takes approximately 400 tons<sup>a</sup> of Te to manufacture the PVs needed to produce one GW of electricity [27]. Since the world's current production for Te is estimated to be 450-500 tons [20], substantial increases in Te production are required to allow for the predicted growth in the production of CdTe PV cells. Te supply concerns coupled with its application in emerging renewable energy applications has led some organizations such as the American Physical Society (APS), U.S. Department of Energy (DOE), and the European Commission Joint Research Centre (JRC), to name Te as an "energy critical element" (ECE) [27-29]. The APS applies the term ECE to elements meeting two requirements: (1) the element is critical to the production of one or more energy related technology that has the ability to impact the way energy is produced, transmitted, stored, or conserved and (2) the element does not have a well-established market because it has not been widely extracted or traded in the past [27].

These issues have led many experts, individuals, and governments to question if global Te supplies will be able to support growing demand of Te for the production of PVs and other end uses. In answer, multiple studies have concluded that the absolute availability of Te is not the limiting factor but rather the fluctuations and possible increases in the price of Te that will likely limit the implementation of CdTe PV cells [14, 15, 22, 30, 31]. While increasing Te production would resolve the issue of Te scarcity, this is not a simple or easy solution because the production of Te is interdependent with and relies on the Cu industry [14].

There are three primary issues limiting Te byproduct production from Cu: (1) Not all Cu extraction operations recover Te, (2) Te extraction efficiencies are low, and (3) an increasing amount of Cu is extracted using SX-EW technology that does not recover Te. It is estimated

---

<sup>a</sup> All uses of "ton" in this work refer to a metric ton or 1000 kg.

that if every mine employing electrorefining decided to extract Te as a byproduct the global production of Te as a byproduct of Cu electrorefining can be increased to about three times the current production [7, 31]. The second limitation to Te production as a Cu byproduct is that overall extraction efficiencies are low. As a specific example, the extraction of Te from Cu anode slimes have been reported as low as 30-40% even though it should be possible to achieve a 80-90% Te extraction efficiency [31]. Third, the demand of Cu has grown at a relatively steady rate of three percent per year in the past 100 years; however, the sources of Cu have changed. Currently only about 65% of Cu is produced by pyrometallurgical extraction electrorefining. The remaining the Cu is either produced by SX-EW or is a product of Cu recycling, neither of which allows for the production of Te [25].

### *1.5 Current Copper Extraction Process*

About 80% of the world's copper production is found in Cu-Fe-S minerals, such as the porphyry deposits of chalcopyrite [23]. Since the majority of Te is extracted as a byproduct of Cu mining, it is key to understand the chemical and physical process that make up the pyrometallurgical Cu extraction prior to examining the behavior of Te within that process. The Cu extraction process can be unique to each mining operation based on parent ore mineralogy, technological evolutions, and government sanctioned environmental regulations [32]. However, there are three principle steps in Cu ore processing: mining, smelting, and refining, as is illustrated in **Figure 1.6**.



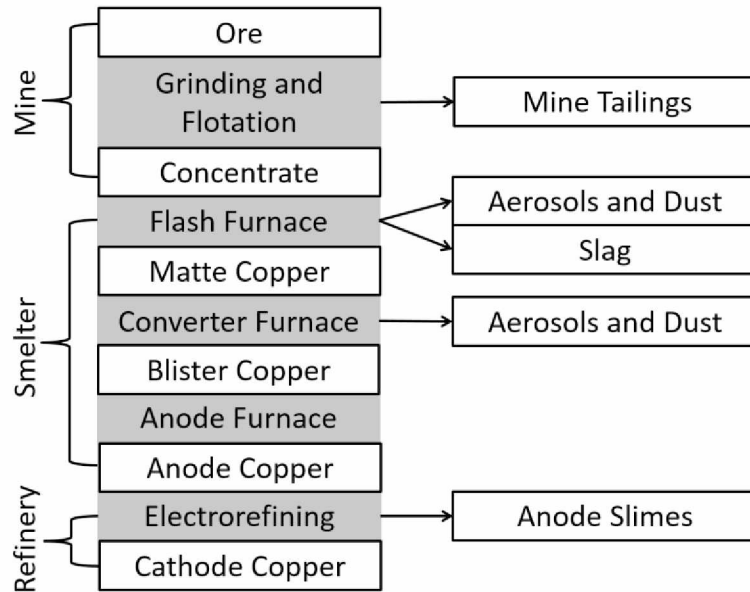


**Figure 1.6** Simple systemic of the Cu mining, smelting, and refining process. The mine tailings, slag, slimes, and gas impurities are all consider to be waste products.

### 1.5.1 Copper Mining

Ore is extracted from the ground at the mine site. For most open pit mines, the ore grade is about 0.5% to 2% copper, which is too low for the ore to be smelted economically; therefore, the Cu in the ore must be concentrated at the mine before it is transferred to the smelter. The ore is first ground to a particle size of  $\sim 250 \mu\text{m}$  (60 mesh). After grinding, the Cu-bearing minerals are concentrated and separated from the non-Cu-bearing minerals, also known as gangue minerals, by a process called froth flotation. During froth flotation, pulverized ore is treated with reagents, called collectors, causing Cu-bearing minerals to repel water. These collectors work because their polar ends will attach to the sulfide mineral surface while the nonpolar hydrocarbon end will extend outward cause the mineral to repel water. The most common sulfide collectors are xanthates such as potassium amyl xanthate, sodium ethyl xanthate, and sodium isopropyl xanthate. As air bubbles are released from the bottom of the tank, causing the Cu-bearing sulfide minerals float to the top while the gangue minerals sink. The concentrate is typically about 30% Cu by mass, recovers about 90% of Cu in the ore, and represents only 1-2 % of the ore material originally taken out of the ground. The minerals that

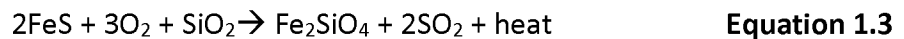
sink to the bottom are known as the mine tailings and are discarded at the mine. The concentrate is then transported to the smelter where it is further refined [23].

### 1.5.2 Copper Smelting

At the smelter, Cu ore is processed to produce Cu anodes. There are three furnaces used to produce Cu anodes from the Cu concentrate: flash furnace, converter, and anode furnace. The first step in the smelting process is to heat the concentrate to >1200° C in the flash furnace in the presence of oxygen gas (O<sub>2</sub>) and silica minerals. In the furnace, the silicates react with the iron oxide (FeO) to produce an iron rich slag (Fe<sub>2</sub>SiO<sub>4</sub>), which is discarded or sold. During the oxidation of sulfide minerals, sulfur dioxide (SO<sub>2</sub>) gas is produced. This gas is harmful to the environment and must be collected and separated from dust and aerosol particles. Therefore, SO<sub>2</sub>(g) is then cleaned and converted to sulfuric acid prior to sale or use on site. The flash furnace partially oxidizes S and Fe and produces a Cu-rich matte (Cu<sub>2</sub>S·FeS), which will be further processed in the converter furnace. **Equations 1.1 and 1.2** give a summary of the chemical processes of the flash furnace.



The Cu-rich matte is then moved into a converter furnace where it is further oxidized to continue separation of Cu from Fe and S. Liquid matte is added to the converter through a large central mouth. The converter is then rotated, which forces oxygen into the matte. The conversion of matte into crude copper takes place in two steps: (1) the Fe elimination step (**Equation 1.3**) and (2) the blister copper formation step, which produces Cu that is 98-99% pure (**Equation 1.4**).



The iron silicate wastes from the converter furnace (Fe<sub>2</sub>SiO<sub>4</sub>) is recycled in the flash furnace because it can contain up to eight percent Cu. Like the flash furnace, the SO<sub>2</sub>(g) is purified and sold or used on site.

The blister copper is then treated in an anode furnace with a non-oxidizing gas (such as methane) to remove excess oxygen and then is poured into copper anode molds. The 98-99% pure Cu anodes will have minor impurities such as gold (Au), silver (Ag), platinum group elements (PGE), Se, and Te. These molds are then sent to the refinery where these impurities are removed [23].

### 1.5.3 Copper Refining

At the refinery, Cu anodes are purified to produce Cu cathodes that are 99.9% pure. Copper cathodes are produced by dissolving the Cu anodes in a  $\text{CuSO}_4 \cdot \text{H}_2\text{SO}_4$  electrolyte solution prior to electrochemically plating Cu onto either steel or copper cathodes (**Figure 1.7**). Impurities such as Au, Ag, PGE, Se, and Te do not dissolve in the electrolyte solution and sink to the bottom to make up the anode slimes [23].

Raw anode slimes, primarily composed of  $\text{CuSO}_4 \cdot 5\text{H}_2\text{O}$ , are subjected to a high pressure, high temperature acidic leach to liberate the Cu. After the Cu is removed, the pressed anode slimes are further processed for the recovery of the precious metals (Au, Ag, and Pt group) and sometimes Se and Te [33].

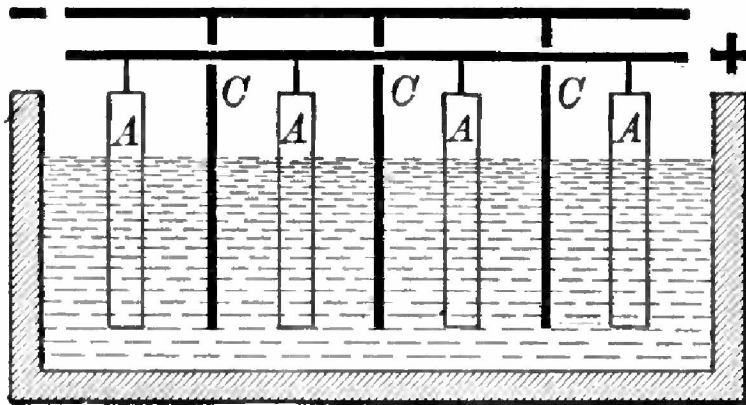


**Figure 1.7** The electrochemical dissolution of Cu anodes in an electrolyte solution. Impurities such as Au, Ag, Pt, Pb, Te, and Se do not dissolve and sink to the bottom and become part of the anode slimes [34].

### 1.6 Tellurium Byproduct Recovery

The mass balance of Te during the mining and smelting process has previously been calculated for a 1970's Russian Cu mining operation (**Figure 1.8**). This study found that the majority of the Te in the original ore did not report to the anode slimes; almost 90% of the Te was lost at the mine during the initial concentration process. Since this study was performed before the invention of modern flash furnaces, this mine used a reverberatory furnace, which did not allow convertor slag recycling. At the smelter, 1.9% of the Te was lost to the furnace slag and 2.6% to the gas cleaning off the furnace. The slag from the convertor removed another 2.4% and 1.3% of the Te was found in the gas cleaning product. A total of 3.2% Te reported to the copper anode slimes were it was refined into pure Te metal and sold [7].

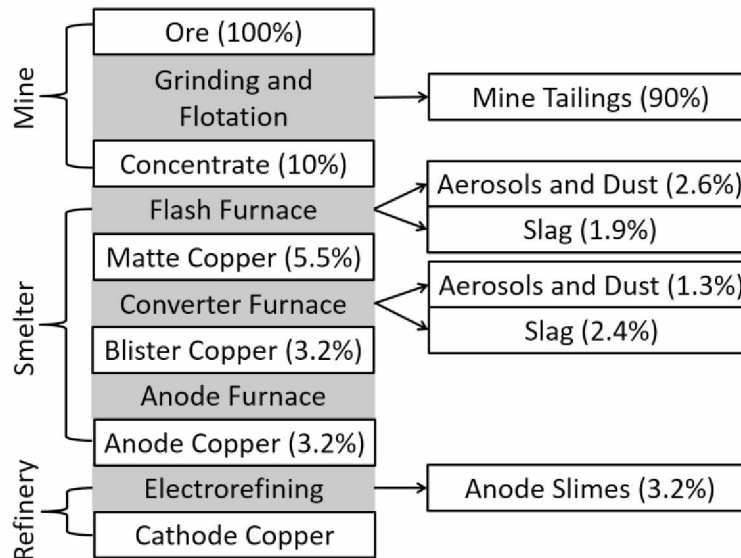


**Figure 1.8** Mass balance of Te for a Russian Cu mine and smelter in the 1970s [7].

#### 1.6.1 Mineralogy of Tellurium in Ore Deposits

Tellurium most often occurs as telluride minerals in copper and gold deposits. In the natural environment, Te has chalcophile tendencies, meaning it is found with sulfide containing minerals such as pyrite ( $\text{FeS}_2$ ) and chalcopyrite ( $\text{CuFeS}_2$ ). Currently, Te has not been detected in rock-forming silicates, however, this may be because the detection limits of analytical methods for Te (in  $\text{mg}\cdot\text{kg}^{-1}$ ) do not allow for the detection of Te rather than the lack of Te in silicates. From a present day economic viewpoint, the most important occurrence of Te is with

chalcopyrite [2]. This is because the majority of commercially available Te is produced as a byproduct of copper mining, mainly the mining of porphyry copper deposits and associated skarns [1]. However, more Te by mass is associated with Au-Ag telluride deposits [2], from which Te is rarely recovered [35].

Most naturally occurring sources of Te occur as a telluride; however, there are a few rare tellurite minerals (**Table 1.1**). Although several tellurate minerals have been described [36], it is believed that tellurates will only occur under exceptional climatic conditions. An examination of an Eh-pH diagram (**Figure 1.9**) shows that  $\text{Te}^{6+}$  will only occur in highly oxidizing conditions. However, oxidized tellurium has also been found in the environment [37]. Unlike sulfite and selenite, tellurite is stable even in oxidizing conditions. Because of their stability, Au-Ag tellurides can accumulate in placer deposits with gold and other heavy minerals [2]. There is some evidence that tellurium can substitute into the matrix of sulfide minerals as evidenced by SIMS data from the Emperor Mine in Fiji where Te has been measured without Au [38]. Tellurium can also occur as native tellurium, and, as mixed S-Te minerals, such as goldfieldite or tetradymite [39].

**Table 1.1** Examples of some Te bearing minerals

<b>Name:</b>	<b>Chemical Formula:</b>
Sylvanite	$(\text{Au}_{1-x}, \text{Ag}_{1-x})\text{Te}_4$
Calaverite	$\text{AuTe}_2$
Krennerite	$(\text{Au}, \text{Ag})\text{Te}_2$
Petzite	$\text{Ag}_3\text{AuTe}_2$
Cervelleite	$\text{Ag}_4\text{TeS}$
Tsumoite	$\text{BiTe}$
Wehrlite	$\text{Bi}_3\text{Te}_2$
Tellurobismuthite	$\text{Bi}_2\text{Te}_3$
Tetradymite	$\text{Bi}_2\text{Te}_2\text{S}$
Altaite	$\text{PbTe}$
Goldfieldite	$\text{Cu}_{12}(\text{Te}, \text{Sb}, \text{As})_4\text{S}_{13}$

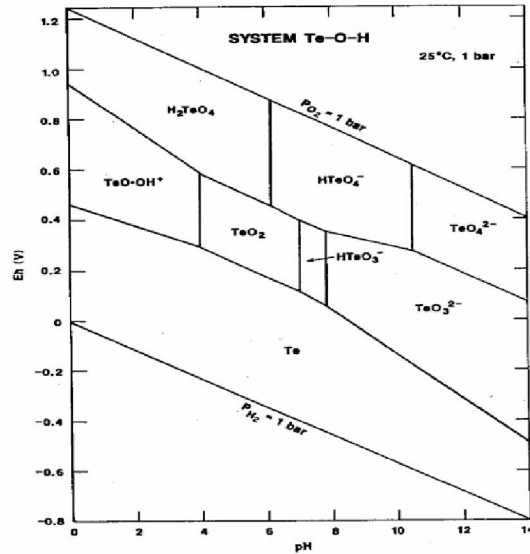


Fig. 5. Eh-pH diagram for part of the system Te-O-H. The activity of dissolved Te =  $10^{-6}$ . See text for discussion

Figure 1.9 Eh-pH diagram of Te aqueous species [40].

Few studies have quantified bulk Te concentrations in copper ore deposits. In an analysis of chalcopyrite from continental porphyry deposits [41], a range of 0 – 220 mg·kg<sup>-1</sup> Te, with an average of 19.6 mg·kg<sup>-1</sup> was determined. Yano (2012) found that the concentration of Te correlates with the concentration of silver (Ag), bismuth (Bi), lead (Pb), and gold (Au), suggesting that Te occurs in chalcopyrite as nanoparticles of telluride minerals rather than in the lattice of chalcopyrite [41]. Reich (2013) found trace amount of Te (~5 mg·kg<sup>-1</sup>) associated with the pyrite constituent of porphyry copper deposits [42].

### 1.6.2 Behavior of Tellurium during Copper Concentration

Knowledge about the behavior of Te during copper ore concentration is limited to the behavior of Au and Ag tellurides which have been studied because of the precious metals associated with Te. Gold tellurides are known to readily float during froth flotation; however, the presence of heavy metal salts will decrease the tendency for Au tellurides to float with chalcopyrite [43].

### 1.6.3 Behavior and Mineralogy of Tellurium in Cooper Anodes and Anode Slimes

The Te concentrations in Cu anodes typically range from 5 to 400 mg·kg<sup>-1</sup>. Tellurium in the anode can occur in a variety of forms. The principle form is as telluride (>85%), in solid solution in the Cu matrix (3-9% Te) and, in high Te anodes, as an oxide phase. The principle telluride phases found in Cu anode include Cu<sub>2</sub>(Se,Te) and (Ag,Cu)<sub>2</sub>(Se,Te), where Te substitutes for Se in the crystal structure. Tellurium occurring in solid solution in the Cu matrix can range from 15 to 92 mg·kg<sup>-1</sup>, with higher concentrations of Te in the Cu anode leading to more Te in solid solution. In high Te anodes, minor amounts of Te can also be found in the Cu-Pb-As-Sb-Bi oxide phase [44].

Currently, little is known about the mineralogy and speciation of Te in the anode slimes. However, this is an active area of research mainly because of the importance of the slimes in the recovery of precious metals [7]. Copper anode slimes typically have a Te concentration of 1% to 5% Te [45]. Because of their fine grain size (<10 μm), heterogeneous nature, and soft, and sometimes amorphous, structure, the anode slimes are difficult to characterize. Therefore it is necessary to use multiple techniques and complex sample preparation to determine the mineralogy of the anode slimes [46].

As the Cu anode is electrochemically dissolved in the CuSO<sub>4</sub>·5H<sub>2</sub>O electrolyte solution, many of the impurities in the anode, such as Ag, Ni, Pb, As, and Sb, also dissolve [44]. However, the majority of the Te remains largely unaffected. The telluride inclusions in the Cu anode drop into the anode slimes, with just a minor amount of Te oxidization. Unlike Te in the Cu<sub>2</sub>(Se,Te) or (Ag,Cu)<sub>2</sub>(Se,Te) phase, Te that exists in solid solution in the Cu matrix will dissolve with the anode and oxidize. However, this Te typically reprecipitates out to form the complex oxidate phase, which is a Cu-Ag-Pb-Au- sulfate-arsenate-antimonate-selenite-tellurite compound. In microprobe studies performed on a Cu anode as it electrochemically dissolves, the backscattered electron image shows the majority telluride phase as a spheroidal, ring-like, or irregular mass in the porous slime matrix (**Figure 1.10**) [47]. Due to the high mean atomic mass, these particles appear bright on the image. The oxidate phase appears less bright, is optically transparent, and has an irregular shape. The ability of Te to dissolve, oxidize, and then

reprecipitate is one of the reasons that the removal of Te from the anode slimes during decopperization is often low and inconsistent.

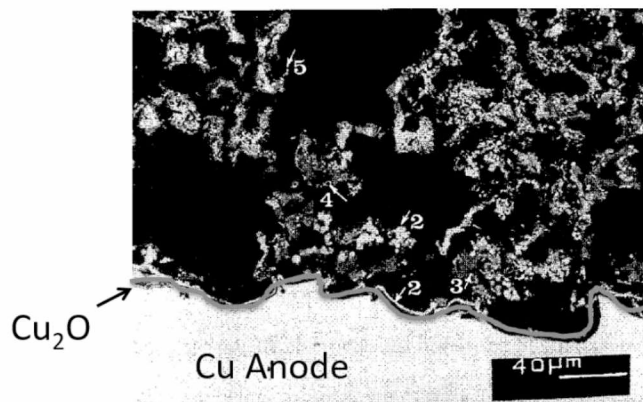
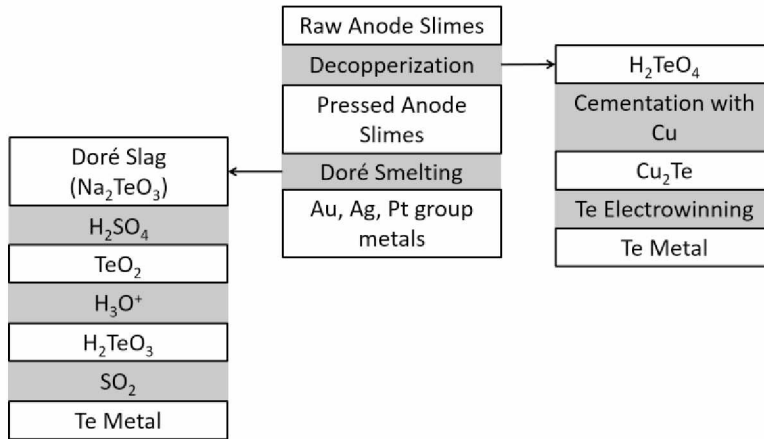


**Figure 1.10** Backscattered electron microscope image of a Cu anode slime as it dissolves electrochemically. Particle 3 is the oxidate phase and particle 4 is (Ag,Cu)<sub>2</sub>(Se,Te) [47].

#### 1.6.4 Extraction of Tellurium as a Copper Byproduct

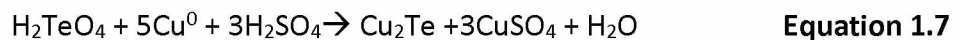
The process used to extract byproducts from the anode slimes is dependent on the mineralogy, speciation, and chemical composition of Au, Ag, PGE, Te and Se in the slimes. Since this can differ from each mine based off the differences in the parent ore and the exact Cu extraction process used, the processing of the slimes differs and is possibly unique for each mining operation [32]. However, there are a few main steps employed by most refineries (**Figure 1.11**) [48]. Because of their consistently high economic value, the current byproduct extraction process has been optimized for the extraction of precious metals often found in the slimes and not for the extraction of Se and Te [7]. The exact efficiency of recovery of Te from the anode slimes varies, and has been reported to average 30-40% for Cu refineries in Europe [31]. It has been estimated that increasing the efficiency of Te extraction from the slimes to around 80% has the potential to double the global production of Te [7].





**Figure 1.11** Processing of Te from raw anode slimes to pure Te metal [32, 48-50].

Before the recovery of the precious metals, the anode slimes are first treated to remove Cu, which accounts for ~5 – 20% by mass of the anode slimes [32]. The decopperization step also generally involves the removal of Te as well [49]. The most common method employed today for decopperization is autoclaving (using high pressure and temperature) in an oxidizing environment and sulfuric acid (H<sub>2</sub>SO<sub>4</sub>) [33]. Autoclaving allows for the removal of nearly 100% of the Cu in the slimes [32]. However, the amount of Te dissolved during autoclaving is inconsistent and often low due to refractory Te compounds in the slimes and the ability of Te to dissolve, oxidize, and then reprecipitate [47]. Tellurium is separated from Cu through cementation with Cu (**Equations 1.5 – 1.7**). Elemental Te (Te<sup>0</sup>) is then extracted from the Cu<sub>2</sub>Te by alkaline leaching and electrowinning (**Figure 1.12**). After the removal of Cu and some Te, autoclaving produces a product known as the pressed slimes [49].



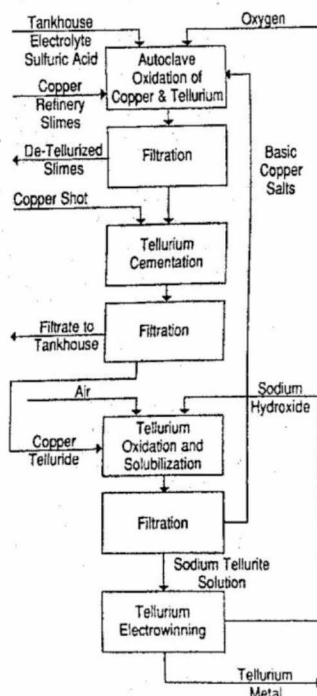
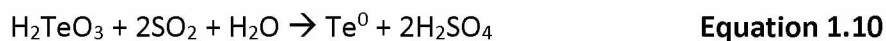
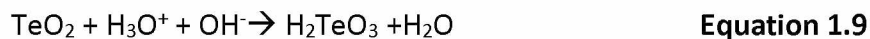
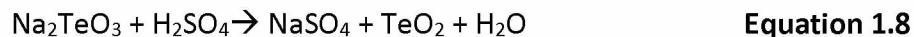


**Figure 1.12** Recovery of Te from leach after autoclave decopperization [49].

As a substantial fraction of the Te remains in the pressed slimes, many refineries will also extract Te from the soda slag of the doré furnace. The doré furnace is the furnace where the pressed slimes are further processed for the extraction of the precious metals [50]. The doré furnace produces a sodium carbonate ( $\text{Na}_2\text{CO}_3$ ) rich slag containing sodium tellurite ( $\text{Na}_2\text{TeO}_3$ ). This soda slag is then pulverized and water leached under slightly acidic conditions ( $\text{pH}=5.5$ ) to precipitate tellurium oxide ( $\text{TeO}_2$ ) (**Equation 1.8**), which is then dissolved in an acid, usually  $\text{H}_2\text{SO}_4$ , to produce tellurous acid ( $\text{H}_2\text{TeO}_3$ ) (**Equation 1.9**). Tellurous acid is treated with  $\text{SO}_2(\text{g})$  to produce  $\text{Te}^0$  (**Equation 1.10**) [48].



### 1.7 Research Objectives

In order for CdTe based PVs to substantially contribute to solving growing global energy demands, a stable affordable source of Te is required [14, 16]. One way to increase Te resources available to industry is to optimize byproduct recovery of Te from Cu extraction. This

requires a fundamental understanding of Te behavior during the Cu extraction process. The American Smelting and Refining Company (ASARCO) is currently the only domestic producer of Te, which is why we have collaborated with them to examine Te behavior during Cu extraction. The specific aims of this project at the ASARCO Mission and Ray Mine, Hayden Smelter, and Amarillo Refinery are as follows:

1. Calculate the mass balance of Te through the Cu extraction process to identify key points in the extraction process to target for optimization of Te extraction
2. Analyze Te's mineralogy and bonding environment in waste products and anode slimes to facilitate development of Te extraction strategies.

In order to address these aims, samples from throughout the ASARCO process from ore to doré furnace soda slag were collected. Elemental composition of each sample was analyzed by inductively coupled plasma mass spectrometry (ICP-MS) and wavelength dispersive x-ray fluorescence (WD-XRF). These concentrations were used to calculate the mass balance of Te at the mine and smelter.

The Te mineralogy and bonding environment of Te were examined with several different techniques. Micro-focused x-ray fluorescence ( $\mu$ -XRF) maps were collected on thin-sections to determine collocated elements, and the UAF electron microprobe (EMPA) was used to determine Te bearing grains in the concentrate and slime samples. The speciation of S and Te, as concentration allowed, were examined by x-ray absorption spectroscopy (XAS). The speciation of S is of interest in this project because S, like Te, is a group 16 element and can exhibit the same oxidation states as Te, and was used to lend insight into Te behavior when Te concentrations were too low to be directly determined.

## Chapter 2 Site Description

The site selected for this project was the American Smelting and Refinery Company (ASARCO), a copper production facility based out Tucson, Arizona. ASARCO is currently the only domestic producer of Te [16]. There are three sites for ASARCO Cu production: (1) the mines, which include the Mission Mine complex and Ray Mine, (2) the Hayden Smelter, and (3) the Amarillo Refinery [51].

### 2.1 The Mines

There are two main mine sites at which ASARCO mines Cu ore, the Mission Mine complex and the Ray Mine. The Mission Mine consist of two mills, the Mission Mine North and Mission Mine South [51]. It is located 32 km southwest of Tucson, AZ in the Pima mining district. The Pima mining district consists of a porphyry Cu and skarn orebody with an average grade of 0.62% Cu [52]. Mining at the Mission complex began in 1916 [51]. The Mission Mine also contains carbonate and sulfide minerals, e.g. Zn, Pb, and Mo sulfides [53]. The Ray Mine is located 113 km north of Tucson, near Hayden, AZ. Mining at the Ray mine began in 1911. Like the Mission Mine complex, the Ray Mine also hosts a porphyry Cu deposit, but unlike Mission Mine, Ray Mine contains no skarn [54]. The mined ore is concentrated on site before it is transported to the smelter.

For this project, ore samples, as well as blast samples from hornfels, diposide-, wollastonite-, and garnet-rich ores from the Mission Mine were obtained. Samples of the concentrate from the Mission Mine North, Mission Mine South, and the Ray Mine were collected, and the flotation head and tails from the Mission North were also collected.

### 2.2 The Smelter

The concentrate from the Mission Mine complex and the Ray Mine, as well as some third party mines, are processed at the Hayden Smelter. The Hayden Smelter is located in Hayden, AZ, near the Ray Mine. The Hayden Smelter processes approximately 27,400 tons of concentrate a day. **Figure 2.1** shows that schematic of the Cu extraction process at Hayden Smelter [51]. For this project, the following samples have been obtained: concentrate, the filter

from the flash furnace, the filter from the converter, and the slag from the flash furnace (indicated by stars in **Figure 2.1**).

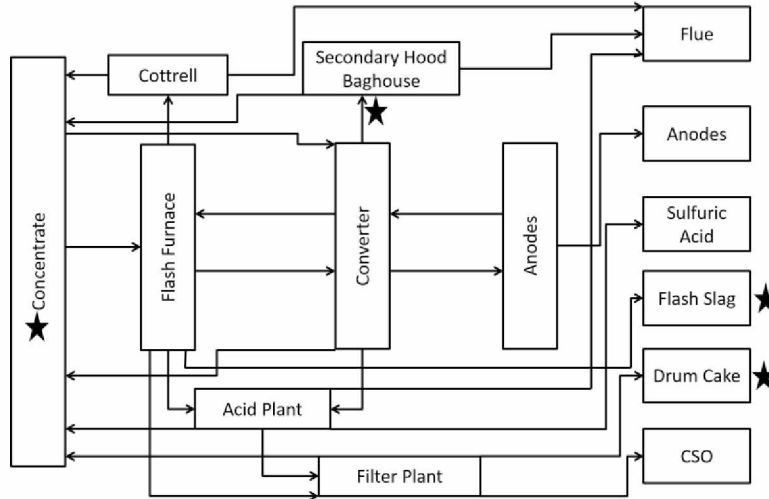


**Figure 2.1** The ASARCO Hayden Smelter diagram. The stars shows the products for which samples were obtained [51].

### 2.3 The Refinery

From the Hayden Smelter, the Cu anodes are transported to the Amarillo Refinery which is located 14 km northeast of Amarillo, TX. The Amarillo Refinery produces refined Cu cathode, silver bars, gold bars, crude nickel sulfate ( $\text{NiSO}_4$ ), Se, Te, Pt sponge, and palladium (Pd) sponge. Sample analyzed from the refinery include: raw anode slimes, pressed anode slimes, doré furnace soda slag and the doré furnace gas filter.

## Chapter 3 Methods

### 3.1 Sample and Standard Collection, Preparation, and Preservation

Samples were collected from ASARCO mines, mills, smelter, and refinery at various steps in the copper extraction process (**Table 3.1**), including: hand samples of ore, blast hole cuttings, mill heads, mill tails or mine tailings, and concentrate from the Mission complex, including both the north and south mills (Sahuarita, AZ). Concentrate samples were also obtained from the Ray mine (Hayden, AZ). Smelter samples were acquired from the Hayden Smelter (Hayden, AZ) and refinery samples were obtained from the Amarillo Refinery (Amarillo, TX).

**Table 3.1** List of ASARCO sample numbers, description, location, and date collected.

Sample #:	Sample Description:	Sample Location:	Date:
335	Garnet (andradite) skarn	Mission Mine	4/10/2012
335-Cp	Chalcopyrite separate of sample 335	Reichardt Building	12/2013
338	Hornfels	Mission Mine	4/10/2012
338-Py	Pyrite separate of sample 338	Reichardt Building	12/2013
342	Hornfels blast hole	Mission Mine	4/10/2012
343	Diposide blast hole	Mission Mine	4/10/2012
344	Diopside blast hole	Mission Mine	4/10/2012
345	Garnet blast hole	Mission Mine	4/10/2012
346	North Mission Mine concentrate	Mission Mine	4/10/2012
347	South Mission Mine concentrate	Mission Mine	4/10/2012
348	Red Hill Pit	Mission Mine	4/10/2012
349	Doré furnace soda slag	Amarillo Refinery	3/29/2012
350	Doré furnace dust	Amarillo Refinery	3/29/2012
351	Flash furnace dust	Hayden Smelter	4/10/2012
352	Ray Mine concentrate	Ray Mine	3/22/2012
353	Convertor dust	Hayden Smelter	4/12/2012
354	Raw slimes	Amarillo Refinery	4/12/2012
355	Pressed slimes	Amarillo Refinery	4/12/2012
416	North Mission Mine flotation head	Mission Mine	3/2013
417	North Mission Mine flotation tail	Mission Mine	3/2013
418	North Mission Mine concentrate	Mission Mine	3/2013
467	Flash furnace slag	Hayden Smelter	2/10/2014

Samples were air dried, many prior to their receipt from ASARCO and stored under ambient conditions prior to analysis. For ICP-MS, WD-XRF, and bulk XAS analysis, samples and

reference materials were ground to a particle size of <10  $\mu\text{m}$  using a McCrone Micronizing Mill located at the University of Alaska Fairbanks (UAF) Advanced Instruments Laboratory (AIL). In the micronizing mill, samples were ground in ethanol for at least 10 minutes using corundum grinding elements. For micro-focused XRF and electron probe microanalysis, thin sections were prepared by embedding unground sample in EPOTEC 301-2FL epoxy and curing under a vacuum for three days, prior to sectioning to 30  $\mu\text{m}$ , polishing on both sides, and then mounting on quartz slides by Spectrum Petrographics (Vancouver, WA).

All reagents used were ACS grade or better. Reference materials were obtained from a variety of different sources as outlined in **Table 3.2**.

**Table 3.2** Sources of S and Te reference compounds

Reference:	Formula:	Source:	ID or location:	Reference:
Ammonium Sulfate	$(\text{NH}_4)_2\text{SO}_4$	Sigma Aldrich	A2939	this study
Anglesite	$\text{PbSO}_4$	Sigma Aldrich	10011KE	Hayes 2014 [55]
Barite	$\text{BaSO}_4$	UAF Museum of the North	AK-1417-G-1	this study
Copper Sulfate Pentahydrate	$\text{CuSO}_4 \cdot 5\text{H}_2\text{O}$	Fishers Chemical		this study
Chalcocite	$\text{Cu}_2\text{S}$	Wards Scientific	14023	this study
Chalcopyrite	$\text{CuFeS}_2$	Wards Scientific	49-5864	this study
Covellite	$\text{CuS}$	Excalibur Mineral Corporation	Butte, Montana	this study
Goslarite	$\text{ZnSO}_4 \cdot 7\text{H}_2\text{O}$	Mallinckrodt	V076116	Hayes 2014
Gypsum	$\text{CaSO}_4 \cdot 2\text{H}_2\text{O}$	Wards Scientific	Alberta, Canada	Hayes 2014
Iron (III) Sulfate	$\text{FeSO}_4$	Fishers Chemical	040692	Hayes 2014
Molybdenite	$\text{MoS}$	Wards Scientific	491686	this study
Pyrite	$\text{FeS}_2$	Wards Scientific	Unknown	Hayes 2014
Pyrrhotite	$\text{Fe}_{1-x}\text{S}$	Wards Scientific	46E4699	this study
Sodium Sulfite	$\text{Na}_2\text{SO}_3$	Sigma Aldrich	S-8018	Hayes 2014
Sodium Sulfate	$\text{Na}_2\text{SO}_4$	Sigma Aldrich	117K0004	Hayes 2014
Troilite	$\text{FeS}$	Excalibur Mineral Corporation	Alta Mine, California	Hayes 2014
Sodium Tellurate	$\text{Na}_2\text{TeO}_4$	Alfa Aesar	AH41778-18	this study
Sodium Tellurite	$\text{Na}_2\text{TeO}_3$	Alfa Aesar	AA75106-18	this study
Tellurium oxide	$\text{TeO}_2$	Alfa Aesar	12284	this study

**Table 3.2** continued

Reference:	Formula:	Source:	ID or location:	Reference:
Native Te	Te	Excalibur Mineral Corporation	USA	this study
Calaverite	AuTe <sub>2</sub>	Excalibur Mineral Corporation	Cresson Mine, USA	this study
Copper Telluride	Cu <sub>2</sub> Te	Alfa Aesar	44077	this study
Tellurobismutite	Bi <sub>2</sub> Te <sub>3</sub>	Excalibur Mineral Corporation	Boliden, Sweden	this study
Pilsenite	Bi <sub>4</sub> Te <sub>3</sub>	Excalibur Mineral Corporation	Hope, B.C. Canada	this study
Tsumoite	BiTe	Excalibur Mineral Corporation	Bjorkdalsgruvan, Sweden	this study

### 3.2 Elemental Analysis

#### 3.2.1 Inductively Coupled Plasma Mass Spectrometry

Inductively coupled plasma mass spectrometry (ICP-MS) is a commonly used technique for the measurement of trace elements in environmental samples because of low parts per trillion ( $\text{ng}\cdot\text{kg}^{-1}$ ) detection limits, small amount of sample required ( $\leq 100$  mg) [56], good precision and accuracy, essentially simultaneous analysis of several elements, and minimal interferences leading to a high degree of selectivity [57]. The Agilent 7500ce ICP-MS (Agilent Technologies, Santa Clara, CA) located at UAF AIL was used for the analysis of Te and other trace elements in the ASARCO samples.

**Figure 3.1** shows an instrument diagram of the ICP-MS. In an ICP-MS, the torch creates a plasma that can atomize and ionize the sample. Argon (Ar) gas is used to generate the plasma because the high ionization energy of Ar (1580 kJ/mol), which is higher than all other elements with the exception of helium (He), neon (Ne), and fluorine (F). This means that the analyte atoms are completely ionized in the plasma by collisions with  $\text{Ar}^+$ , excited Ar atoms, or energetic electrons. The ions and plasma will then travel through a series of cones used to steer and condition the ion beam as well as facilitate the decrease in pressure required to prevent collisions between the analyte ions and gas molecules. The first of these is the sampling cone, which has a 1 mm opening and will only allow for a fraction of the plasma to



pass through it. Next, the plasma will pass through a skimmer cone, which has a negatively charged extraction lens placed behind. This lens serves to attract the positively charged ions from the plasma. These ions will then travel through a collision cell that will contain either He gas, or H<sub>2</sub> gas that reduces interferences and guides the ions to the mass separator [58]. Ions are then separated by their mass-to-charge ( $m/z$ ) ratio by a quadrupole mass analyzer. Once the quadrupole has separated the ions, an electron multiplier produces a mass spectrum of the ion counts vs.  $m/z$ . This spectrum is then used to calculate the concentration of analyte [57].

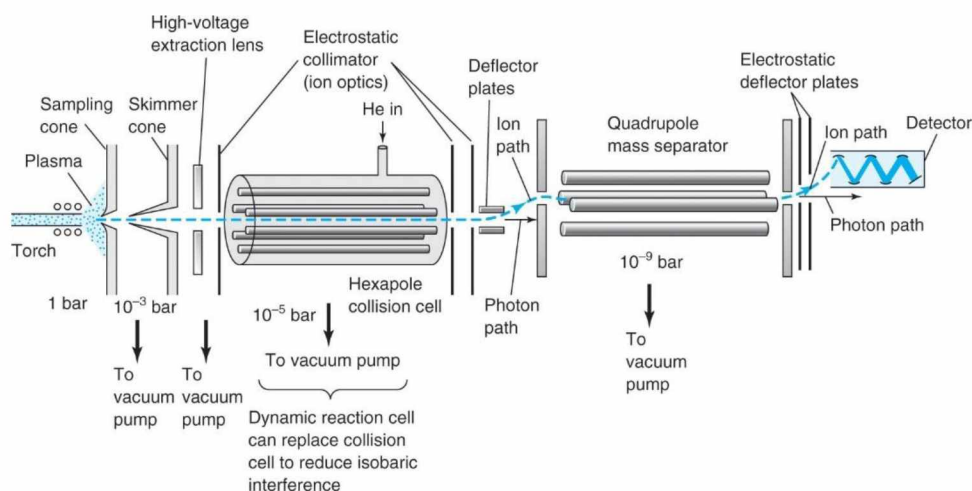


**Figure 3.1** Sample path for ICP-MS analysis [58].

One of the major disadvantage to using ICP-MS is that only aqueous samples may be introduced into the instrument. In geochemical samples, this poses a problem because many naturally occurring samples do not readily dissolve. This leads to some potential barrier in ICP-MS sample preparation including incomplete dissolution and increased sample preparation costs. Other areas of concern for ICP-MS analysis include matrix effects, drift, and memory. Matrix effects is when an element is effected by the presence of other dissolved solids or acids. Drift is seen when the instrument response to an element varies over time and is often the result of changes in instrument parameters. Memory problems occur in cases where the sensitivity is decreased because the previous sample remains in the instrument.

There are three main calibration strategies that can be applied to ICP-MS: external calibration, internal standardization, and standard additions. External calibration uses solutions

of known concentrations to make a calibration curve that can be used to relate signal intensities to the concentration in unknown samples. Internal standardization is the consistent addition to the sample of an internal standard, a solution that contains one or more elements not present in the sample. A good internal standard will contain elements that are closely matched in mass and first ionization potential of the analytes. However, the application of internal standardization is difficult for environmental samples because it cannot always be assumed that the samples does not contain the elements in the internal standard and it can be difficult to find an internal standard recipe that will match the masses of the range of elements of interest. Lastly, standard additions is the addition of the known spike to the unknown samples. This is the most expensive calibration strategy because it requires at least two measurements for every sample. Ideally, the spike solution should contain significantly, roughly five times, more analyte than the sample [56]. Standard additions is the best method of calibration to correct for significant matrix effect problems; however, this correction is best applied to rotational matrix effects, which is where the size of the signal for the analyte is affected by other constituents in the solution. This will affect the slope of the calibration line but not its intercept. Translational matrix effects, which affect the intercept of the calibration and are caused by concomitant substance in the solution, must be corrected with background removal [59].

#### *3.2.1.1 Method Development of Sodium Peroxide Sinter*

In order to dissolve geomeia for ICP-MS analysis, a sample preparation method capable of complete and consistent sample dissolution is critical [60]. Currently, the standard geochemical method is wet chemical digestion using a mixture of concentrated hydrofluoric acid (HF), nitric acid (HNO<sub>3</sub>), and hydrochloric acid (HCl) and perchloric acid (HClO<sub>4</sub>). However, this method is hazardous because of the risks associated with concentrated acids, especially the human health risks associated with HF and the explosive nature of HClO<sub>4</sub>. Although routine at many contract labs, an acid digest procedure is not suitable for the university laboratory environment.

Sodium peroxide ( $\text{Na}_2\text{O}_2$ ) sinter presents an attractive alternative to traditional four acid chemical digestion because, although  $\text{Na}_2\text{O}_2$  is a strong oxidizer, the overall risks are considered lower [60]. Multiple studies have evaluated the accuracy of using  $\text{Na}_2\text{O}_2$  for dissolving samples and compared the peroxide sinter technique with other methods [56, 60, 61]. In particular, Meisel et al. (2002), demonstrated the method suitability for a variety of normal silicate rock through the analysis of several standard reference materials (SRM). The results indicate that peroxide method is both precise (within 5% standard deviation) and accurate for most elements for normal rocks [61].

For  $\text{Na}_2\text{O}_2$  method development, matrix matched Te-containing SRM were selected. These are the National Institute of Standards and Technology (NIST) 2780 Hard Rock Mine Waste and the Natural Resources Canada, CCU-1d, a copper mine concentrate, with 5 and  $36.7 \pm 7.4 \text{ mg kg}^{-1}$  Te, respectively. It should be noted that the NIST 2780 Te values were reported for informational purposes only. As discussed later, the concentrations of trace elements of interest, especially Te, were reliably measured using the peroxide sinter method. Ten replicate measurements of each SRM were performed and yielded results that differed from reported values by less than 10% for Te. Thus, this method was deemed appropriate for use in this study

#### *3.2.1.2 Sample Preparation for ICP-MS*

Samples were prepared for ICP-MS analysis using the sodium peroxide sinter method outlined in Meisel, 2002 [61]. Briefly, in a glassy carbon crucible  $100 \pm 1 \text{ mg}$  of sample and  $600 \pm 5 \text{ mg}$  of  $\text{Na}_2\text{O}_2$  were mixed together. The crucible was then placed in a preheated muffle furnace at  $480 \text{ }^\circ\text{C}$  for 30 minutes. After heating, the crucible was removed from the furnace and allowed to cool to room temperature (approximately 30 minutes). Crucible and clinker were then placed in a 250 mL bottle and then 10 g of 18 M $\Omega$  water was added to the crucible and allowed to react. The reaction often produced small amounts of gas and took about 10 minutes to go to completion, as indicated by the ceasing of bubble formation. At this point the sample and crucible were stored until analysis. On day of analysis 2 g of 13%  $\text{HNO}_3$  and 2 g of 35% HCl were added to the bottle that contained the crucible. Ultrapure water was then added

to bring the total solution mass up to 100 g, prior to final dilution (10x and 500x) and analysis by ICP-MS [61].

### 3.2.1.3 ICP-MS Elemental Analysis

Calibration of the ICP-MS for these analyses involved the use of external calibration, internal standards, and standard addition. External standards used during this procedure to calibrate instrument response with concentrations of elements of interest. The concentrations of the external calibration curve for high concentration elements were 500, 250, 50, 10, 5, and 0.1  $\mu\text{g}\cdot\text{kg}^{-1}$  for Ca, Ti, and Zn. Lower concentration elements were calibrated at 50, 25, 5, 1, 0.5, and 0.1  $\mu\text{g}\cdot\text{kg}^{-1}$  for As, Ba, Bi, Cd, Cr, Au, Mn, Ni, Pb, Pd, Pt, Se, Ag, Te, and V. A mixture of internal standards was added to each sample and standard containing 100  $\mu\text{g}\cdot\text{kg}^{-1}$  of Ge 72, Y 89, Rh 103, and Ir 193. These internal standards were used to constrain calibration curves and check for instrument drift. Each external calibration curve was constrained by the internal standard that gave the best calibration ( $R^2$  closest to 1, for all elements  $R^2 \geq 0.98$ ). Appropriate method and reagent blanks were also measured. During data collection, quality control measures included calibration checks of a mid-calibration standard, blank measurements, and SRM solutions were measured every 10-12 samples.

Standard additions were used to account for matrix effects from the samples and instrumental drift, which were found to be significant during early data collection. A spike solution would ideally contain 5x predicted sample concentration [59]. The higher concentration elements (Ca, Zn, Pb, Ti, Mn, Bi, and Ba) were diluted 500x. An additional 500x dilution of sample was made by diluting 0.5 g of sample and 0.5 g spike solution to a final total mass of 10 g. The 500-fold dilution spike solution contained 100  $\text{mg}\cdot\text{kg}^{-1}$  Ca and Zn, 10  $\text{mg}\cdot\text{kg}^{-1}$  Pb, Ti, and Mn, 5  $\text{mg}\cdot\text{kg}^{-1}$  Bi, 2  $\text{mg}\cdot\text{kg}^{-1}$  Ba, and 0.2  $\text{mg}\cdot\text{kg}^{-1}$  As and Ag. Lower concentration elements (V, Cd, Cr, Bi, Ni, Se, Te, As, Au, Pt, Pd, and Ag) were diluted 10x. In addition a 10x sample was prepared with 0.5 g of sample and 0.5 mL a spike solution diluted to a total mass of 10 g. The ten-fold dilution spike solution contained 3  $\text{mg}\cdot\text{kg}^{-1}$  V, 1.5  $\text{mg}\cdot\text{kg}^{-1}$  Cd and Cr, 1  $\text{mg}\cdot\text{kg}^{-1}$  Bi, Ni, Se, Te, and As, and 0.2  $\text{mg}\cdot\text{kg}^{-1}$  Au, Pt, Pd, and Ag. Spike concentrations were selected to

be 5x the expected sample concentration, although this was not always the case due to sample heterogeneity.

During ICP-MS analysis, measurements of an acid blank, a calibration check, and of NIST 2780 or CCU-1d were taken every 10-12 samples throughout the run to assure the precision and accuracy of results. All measurements were taken in three gas modes: hydrogen, helium, and no gas in the collision cell. The data reported here was collected using hydrogen, and was used because it gave the most accurate and precise quantification of Te.

### 3.2.2 Wavelength Dispersive X-Ray Fluorescence

Wavelength dispersive x-ray fluorescence (WD-XRF) is an excellent method for quantitative elemental analysis of major elements. It is often the method of choice for quantifying elements in solid samples because it can be done relatively quickly, it is nondestructive technique, and is substantially less costly than analysis by ICP-MS [56]. However, the WD-XRF has a higher detection limit than ICP-MS [in the low parts per million ( $\text{mg}\cdot\text{kg}^{-1}$ )] and generally requires at least 10 grams of sample [57]. Wavelength dispersive x-ray fluorescence can be employed to measure both major elements (Na, S, Mg, Al, Si, P, K, Ca, Ti, Mn, Fe etc.) and minor elements (Sr, Zr, Cr, Ni, Cu, Zn, Ba, etc.) simultaneously. A wavelength dispersive spectrometer (WDS) was selected for this study over energy dispersive spectrometer (EDS), because of lower detection limits and higher accuracy and precision [62].

When an atom is hit by a beam of x-ray radiation with energy higher than its ionization potential, a core electron may be ejected from the atom, and the hole will be filled by an electron from a higher shell. This movement of the electron from greater potential to lower potential may also yield a fluorescent photon with a characteristic energy unique to both the transition of the electron and the emitting element. Emission of fluorescent x-rays is not the only possible result of x-ray sample interaction, but is the most probable result for high atomic number ( $Z$ ) elements. X-ray intensity is proportional to elemental concentration in the sample, and thus can be used to quantify elements in the sample. This wavelength of this radiation can be calculated by using **Equation 3.1**.

$$\lambda = \frac{hc}{E} \qquad \text{Equation 3.1}$$

Where  $\lambda$  is the wavelength,  $h$  is Plank's constant ( $6.626 \times 10^{-34} \text{ m}^2 \cdot \text{kg} \cdot \text{s}^{-1}$ ),  $c$  is the speed of light ( $3.00 \times 10^8 \text{ m} \cdot \text{s}^{-1}$ ), and  $E$  is the energy of the absorbed radiation in joules.

In order to be detected by a WD-XRF, fluorescent x-rays generated in the sample must satisfy the diffraction condition, scatter off the detector crystal in order to reach the detector. The angle of the detector crystal and position of the detector are determined by Bragg's Law (Equation 3.2).

$$2d\sin\theta = n\lambda \quad \text{Equation 3.2}$$

These photons are then detected by a scintillation counter. In a wavelength dispersive analysis, characteristic radiation emitted from the sample is selected on the basis of wavelength. Since the count rate is related to the amount of analyte in the sample, this information establishes the elemental composition of the sample and quantifies the concentration of those elements (Figure 3.2) [63].

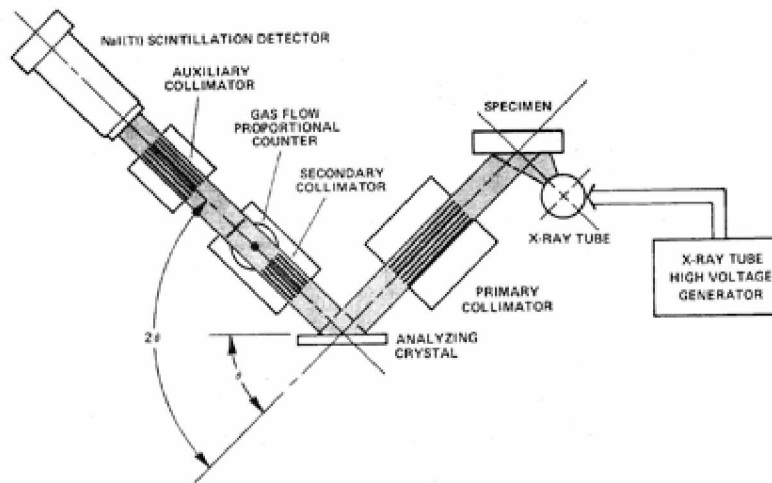


Figure 3.2 Path of x-rays during WD-XRF analysis [63].

### 3.2.2.1 Sample Preparation and Analysis of WD-XRF

Samples for WD-XRF analysis were prepared as pressed pellets by mixing 12.5 g of sample (ground in a steel ball mill) with 1.25 g of PXR-225 (a binding agent) and 7 mL of Vertrel XF (a lubrication agent) for four minutes. The sample, binder, and lubricant ratio has been optimized for samples that contain over 50% sulfide minerals and results in the sample being

diluted by 9%. The sample was then pressed in a 37mm metal cup to approximately 20,000 psi for 2 minutes.

Wavelength dispersive x-ray fluorescence data was collected on a four kilowatt PanAnalytical Axios (Westborough, MA) located in AIL at UAF. The instrument was equipped with a LiF 220 crystal, a scintillation detector, and a 150  $\mu\text{m}$  collimator. The energy was set to 60 keV and the current was 66 mA. For Te, the  $K_{\alpha}$  line was measured at  $18.2^{\circ} 2\theta$  for 188 seconds, while the background was measured at  $17.9^{\circ} 2\theta$  and  $18.7^{\circ} 2\theta$  for 60 and 40 seconds respectively. X-ray fluorescence data was analyzed using PANalytical software, SuperQ (version 4.0Q; 4.1251.3). Spectrum were initially identified with IQ+ (a feature of the software) and then confirmed by manual inspection.

### *3.3 Mass Balance Calculations*

Mass balance calculations were used to determine Te behavior, distribution, and losses during Cu extraction. The mass balance at the mine was calculated using Te concentrations determined by peroxide sinter ICP-MS for samples Mission Mine samples collected April 2012 (samples 416 – 418) and the flux numbers reported by ASARCO for April 2012. For the Hayden Smelter, the mass balance was calculated using ICP-MS concentrations for smelter samples (351, 353, and 467) and flux numbers for March 2010. Mass balance calculations for Te were modeled after bismuth mass balance calculations supplied by ASARCO. The amount of Te in each product and waste product was calculated by **Equation 3.3**.

$$\text{concentration of Te (mg}\cdot\text{kg}^{-1}) \times \text{amount produced (kg)} = \text{amount of Te (mg)}$$

**Equation 3.3**

The amount of Te was then normalized to 100% in the ore so that the data could be reported as percentages. The error associated with the mass balance calculations was calculated by propagation of uncertainty as outlined by Harris (2010) [58].

### *3.4 X-Ray Absorption Spectroscopy*

X-ray absorption spectroscopy (XAS) was used to examine the speciation of Te and S [64]. Synchrotron radiation is needed for XAS in environmental samples because the high

intensity source of x-rays (five to ten orders of magnitude brighter than x-rays produced from a sealed or rotation anode tube) is needed to measure the absorption of the x-rays at the element's characteristic absorption energy in environmental samples. X-ray absorption spectroscopy has been used to study the geochemistry of environmental samples since the 1980's and is now widely used in the field of low temperature geochemistry to probe the speciation of specific elements with low matrix interferences [65, 66].

In a transmission XAS experiment, a monochromatic x-ray beam, which is scanned in energy during the experiment, impinges upon the sample. Some of these x-rays will be absorbed by atoms of the element of interest within the sample and cause the ejection of a core electron. The amount of x-ray absorption is quantified by comparing the intensity of the incident beam to the energy of the transmitted beam. The energy of the transmitted beam can be related to the incident beam by **Equation 3.3**.

$$I=I_0e^{-\mu\rho x} \qquad \text{Equation 3.3}$$

Where I is the energy of the transmitted beam,  $I_0$  is the energy of the incident beam,  $\mu$  is the mass absorption coefficient,  $\rho$  is the density of the sample, and x is the thickness of the sample.

In the case of low concentration samples, fluorescence geometry is preferred to take advantage of inherent sensitivity of fluorescent geometry. Fluorescence photons, of characteristic energy, are produced when a valance electron fills that core hole created by the absorption of the incident x-ray and ejection of a core election (**Figure 3.3**). The fluorescence XAS spectrum exhibits the same shape as a function of excitation energy as the absorption spectrum, meaning the spectra collected using both detection methods can be used interchangeably.



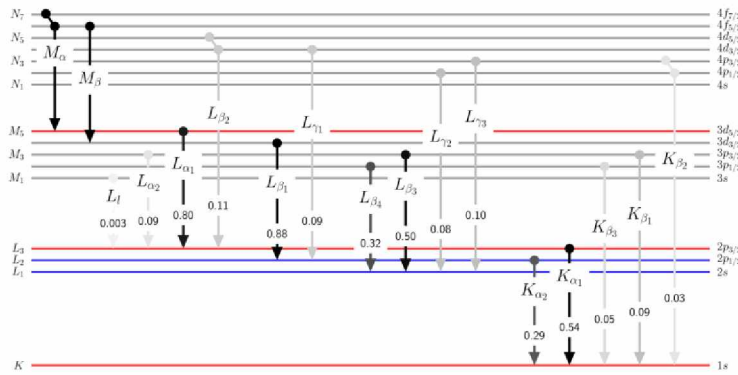


**Figure 3.3** Possible energy transitions elements can undergo that will cause the release of a photon [67]

The XAS spectrum is generally divided into the x-ray absorption near edge structure (XANES) and the extended x-ray absorption fine structure (EXAFS). The phenomena recorded in the XANES region is caused by long range electronic transitions within the atom and multiple scattering of released photons by the atoms surrounding the atom of interest [66] and is sensitive to the oxidation state and mineral phase of the absorbing element [64]. The XANES spectrum is caused by the electron transition happening within the atom and multiple scattering of released photons by the atoms surrounding the atom of interest [66]. The EXAFS region lends insight into the local structure and bonding environment of the absorbing element. It can be used to determine the coordination number, bond lengths, and identity of neighboring atoms [64]. The unique patterns of the EXAFS are a result of the single and multiple scattering of photoelectrons released by neighboring atoms [66].

### 3.4.1 Bulk S XAS

#### 3.4.1.1 Bulk S XAS Collection

Sulfur speciation can be readily probed with known S XAS (also known as NEXAFS for near-edge x-ray absorption fine structure) because of a 12 eV separation of sulfide ( $S^{2-}$ ) and sulfate ( $SO_4^{2-}$ ) oxidation states. Linear combination fits (LCFs) are commonly used for this type of analysis. However, in order to achieve good fits, the sample must consist of a mixture of pure compounds for which reference spectra are available. Linear combination fits can be used

to quantify the ratio of oxidized to reduced species present in the sample. The measurement of S XAS is more complicated than that of heavier elements because low energy x-rays are readily absorbed by air necessitating S XAS experiments to be performed in a He atmosphere.

Sulfur K-edge spectra for samples and reference materials were collected at the Stanford Synchrotron Radiation Lightsource (SSRL) on beam line 4-3. All measurements of the samples were made with a 2 mm vertical slit and a passivated implanted planar silicon (PIPS) detector. Fluorescence geometry was used to measure all references and samples. The energy of the incident x-ray beam was scanned for the pre-edge region (2240 eV to 2800 eV, with a step size of 5 eV), for the edge region (2,240 to 2450 with 0.15 eV steps), and for the post-edge region (2500 to 2800 eV at 0.5 eV steps).

#### 3.4.1.2 S XAS Data Analysis

The XAS spectra for sulfur were averaged and analyzed using SixPACK (version 1.00) [68]. Sulfur energy was calibrated using sodium thiosulfate by setting  $E^0$  to 2472.02 at the maximum of the first peak. To optimize the fits, background was removed by the parameters listed in **Table 3.3** using linear pre-edge fit and a quadratic post-edge fit.

**Table 3.3** Background removal parameters for S XAS analysis

<b>Sample:</b>	<b>Pre-Edge:</b>	<b>Normalization:</b>
349: ACR Slag	-200 to -20	40 to ~330
351: Presscake	-200 to -20	35 to ~330
353: Baghouse Feed	-200 to -20	35 to ~330
354: Raw Slimes	-200 to -20	35 to ~330
355: Pressed Slimes	-200 to -20	35 to ~330
Aluminum Sulfate	-200 to -20	35 to ~105
Ammonium Sulfate	-200 to -20	35 to ~105
Anglesite	-200 to -20	35 to ~105
Barite	-200 to -25	40 to ~105
Chalcanthite	-200 to -25	40 to ~105
Chalcocite	-200 to -25	30 to ~330
Chalcopyrite	-200 to -20	40 to ~105
Covellite	-200 to -25	30 to ~105
Goslarite	-200 to -20	35 to ~105
Gypsum	-200 to -20	35 to ~105
Melanterite	-200 to -20	35 to ~105

**Table 3.3** continued

<b>Sample:</b>	<b>Pre-Edge:</b>	<b>Normalization:</b>
Molybdenite	-200 to -25	40 to ~105
Pyrite	-200 to -10	35 to ~105
Pyrrhotite	-200 to -25	20 to ~105
Sodium Sulfite	-200 to -20	35 to ~330
Thenardite	-200 to -20	35 to ~330
Troilite	-200 to -25	40 to ~330

### 3.4.1.3 S Linear Combination Fitting

After the background was removed, LCFs were performed to determine the individual S components of the system. A library of 17 S reference spectra (**Figures 3.4 and 3.5; Table 3.3**) was initially used to fit each sample spectrum, but fits were eventually constrained by the sample's chemical composition (known from ICP-MS and WD-XRF results), which limited the possible S species to sulfides (covellite, chalcopyrite, chalcocite, and troilite), disulfides (pyrite), and sulfate (barite and chalcantite). The fits were performed using the cycle fitting function within the LCF module within SixPACK. The fits were constrained to non-negative fits only but were not forced to a sum of one. The final fits were selected based on statistics (low reduced  $\chi^2$ ) and knowledge of chemical composition. These fits should be interpreted as a guide for the types of sulfur present in the samples (e.g., sulfides, disulfides, sulfates) rather than a specific indicator of a particular species being present.

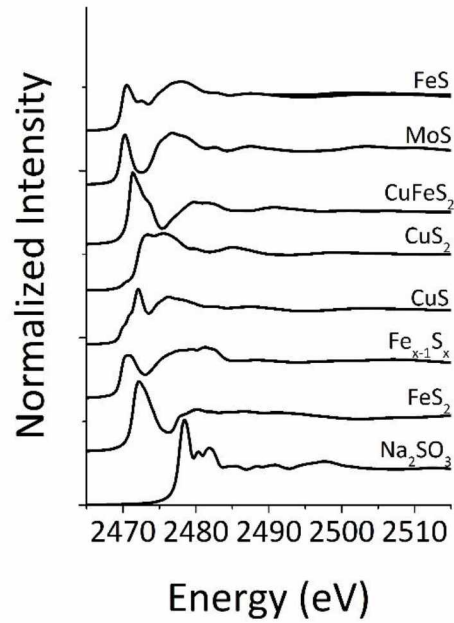


Figure 3.4 XAS spectra for reduced and partially oxidized sulfur reference samples.

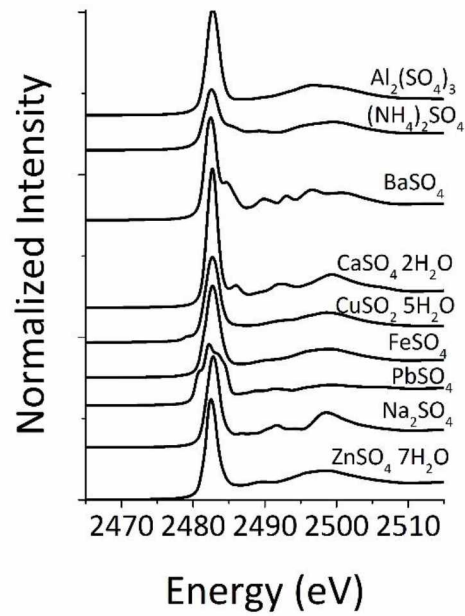


Figure 3.5 XAS spectra for fully oxidized sulfur reference samples.

### 3.4.2 Bulk Te XAS

### 3.4.2.1 Bulk Te XAS Collection

Tellurium K-edge spectra for samples and reference materials were collected at the SSRL on beam lines 4-1 and 11-2. The measurements of reference spectra  $\text{TeO}_2$ , native Te,  $\text{Na}_2\text{TeO}_4$ ,  $\text{Na}_2\text{TeO}_3$ , and  $\text{AuTe}_2$  as well as the raw and pressed slimes and the doré dust and soda slag were made with a 2 mm vertical slit. Reference materials  $\text{Na}_2\text{TeO}_4$ ,  $\text{Na}_2\text{TeO}_3$ ,  $\text{Cu}_2\text{Te}$ ,  $\text{Bi}_2\text{Te}_3$ ,  $\text{Bi}_4\text{Te}_3$ , and  $\text{BiTe}$  and the flash furnace dust measurements were made with a 0.5 mm vertical slit. References were collected in transmission geometry with ion chambers filled with Ar gas, while samples were collected in fluorescence geometry with either a lytle detector or 100-element Ge detector. All experiments were performed at a temperature of 70 K (using liquid nitrogen to cool the chamber). The x-ray excitation energy was scanned for the pre-edge region (31,580 eV to 32,900 eV, with a step size of 5 eV), for the edge region (31,580 to 31,800 at 0.5 eV steps), and for the post-edge region (31,850 to 32,900 eV at 1 eV steps).

### 3.4.2.2 Te XAS Data Analysis

The XAS spectra for Te were averaged and analyzed using SixPACK (1.00) [68]. Tellurium energy was calibrated using tellurium oxide ( $\text{TeO}_2$ ) by setting  $E^0$  to 31,814 eV at the maximum of the first derivative. To optimize the fits, background was removed by the parameters listed in **Table 3.4** using linear pre-edge fit and a quadratic post-edge fit.

**Table 3.4** Background removal parameters for Te XAS analysis

<b>Sample:</b>	<b>Pre-Edge:</b>	<b>Normalization:</b>
Flash Furnace Dust	-200 to -50	100 to ~800
Raw Slimes	-200 to -50	100 to ~800
Pressed Slimes	-200 to -50	100 to ~800
Doré Furnace Slag	-200 to -50	100 to ~800
Doré Furnace Dust	-200 to -50	100 to ~800
$\text{Na}_2\text{TeO}_4$	-200 to -50	100 to ~800
$\text{Na}_2\text{TeO}_3$	-200 to -50	100 to ~800
$\text{TeO}_2$	-200 to -50	50 to ~800
Native Te	-200 to -50	50 to ~800
$\text{AuTe}_2$	-200 to -50	50 to ~800
$\text{Cu}_2\text{Te}$	-200 to -50	50 to ~800
$\text{Bi}_2\text{Te}_3$	-200 to -50	50 to ~800
$\text{Bi}_4\text{Te}_3$	-200 to -30	100 to ~800

Table 3.4 continued

Sample:	Pre-Edge:	Normalization:
BiTe	-200 to -50	50 to ~800

### 3.4.2.3 Te Linear Combination Fitting

After the background was removed, LCFs was performed to determine the distribution of oxidized and reduced Te in the system. A library of 9 Te reference spectra (Figure 3.6; Table 3.4) was used to fit the sample's spectrum. This was done using the cycle fitting function of SixPACK over a range 31800 – 31920 eV. The fits were constrained to non-negative fits only but were not forced to a sum of one. After iterative fitting, the final fits were selected based on statistics (low reduced  $\chi^2$ ).

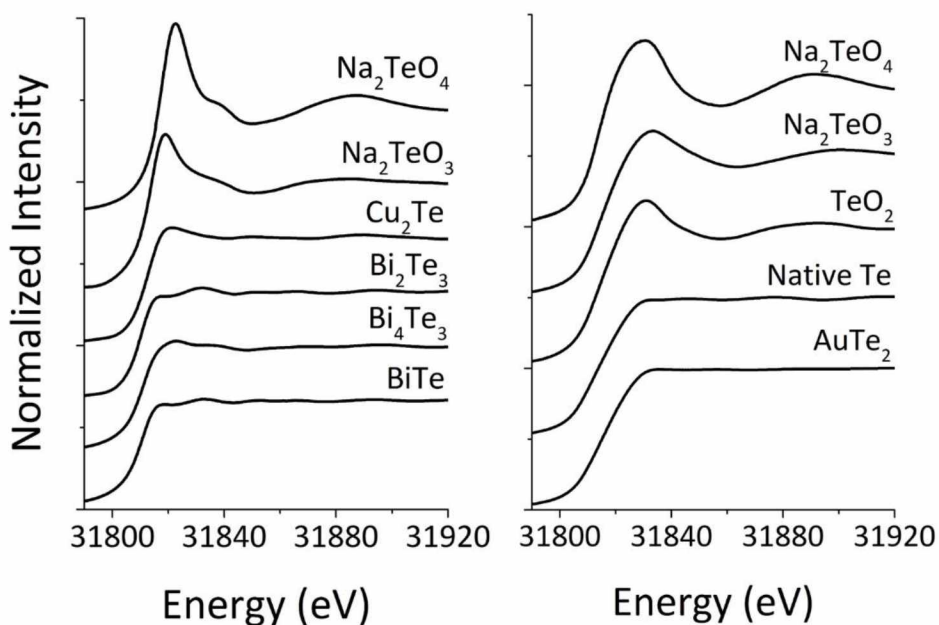


Figure 3.6 XAS spectra for Te reference samples used in LCF. The right graph displays references collected with 0.5 mm slits and the left graph displays references collected with 2 mm slits

### 3.5 Micro-Focused X-Ray Fluorescence Map Collection and Analysis

Examination of chemical composition across or within a single grain with a high degree of sensitivity and high spatial resolution is highly desirable in many contexts. The high

brightness and brilliance of synchrotron light sources leads to the production of small, but intense, x-rays allows for a high degree of sensitivity and spatial resolution synchrotron based XRF mapping is ideally suited to such examination as spots sizes for micro-focused x-ray fluorescence ( $\mu$ -XRF) maps are often only a few  $\mu\text{m}$  and the chemical sensitivities can be less than  $1 \text{ mg}\cdot\text{kg}^{-1}$  [69]. An energy dispersive detector is used to detect x-ray fluorescence in this type of experiment, but the relatively poor energy resolution of this type of detector ( $\sim 100 \text{ eV}$ ) can sometimes not resolve overlaps in emission lines. In this project, it was difficult to resolve the closely spaced Ca  $K\alpha_1$  (3,692 eV) emission line and the Te  $L\alpha_1$  (3,769 eV) [70]. This issue was resolved, for samples with low calcium, through careful windowing and examination of Te and Ca pure standards to deconvolute the Te and Ca signals. Also, the map energy was collected at 7110 eV so that the Fe associated with chalcopyrite would appear brighter than the Fe associated with pyrite [71].

### *3.5.1 Experimental Conditions*

X-ray fluorescence elemental maps were collected at SSRL using beam line 10-2 equipped with a double-crystal monochromator (Si 111  $\Phi=90$ ) used to tune the incident x-ray beam to 7110 eV with a beam current of 500 mA. Beam attenuation filters before  $I_0$  was adjusted so that  $I_0$  was between 0.5 and 2 and in an effort to avoid saturation of the vortex detector. The beam line was configured in fluorescence geometry with the sample placed at 45 degrees to the incident beam and detector. The beam was focused to a spot size of 25  $\mu\text{m}$  with a dwell time of 100 microseconds per point.

Distinguishing between Ca and Te began with creating several energy windows from 3,550 to 4,350 eV with the aim of separating the emissions of Ca from Te (**Table 3.5**). It was determined that window 7 was best at isolating the Te signal based on examination of Te counts in each window in maps of a Ca standard. This is because this window had the least amount of overlap with Ca, without interference from the Ti and Ba emission lines (**Table 3.6**).

**Table 3.5** Energy windows used to examine Te

Window:	Energy (eV):
Te 1:	3550 – 3650
Te 2:	3650 – 3750
Te 3:	3750 – 3850
Te 4:	3850 – 3950
Te 5:	3950 – 4050
Te 6:	4050 – 4150
Te 7:	4150 – 4250
Te 8:	4250 – 4350

**Table 3.6** Emission energies for elements with potential interferences with Te overlap [70]

Element	Emission Line (eV)	Relative Intensity
Sb	$L\alpha_1=3604.72$	100
	$L\alpha_2=3595.32$	11
Ca	$K\alpha_1=3691.7$	100
	$K\alpha_2=3688.1$	50
Te	$L\alpha_1=3769.3$	100
	$L\alpha_2=3758.8$	11
	$L\beta_1=4029.6$	61
Ba	$L\alpha_1=4466.3$	100
	$L\alpha_2=4450.9$	11
Ti	$K\alpha_1=4510.8$	100
	$K\alpha_2=4504.9$	50

### 3.5.2 Map Analysis

To deconvolute Te and Ca peaks, Te and Ca standards were measured and the overlap was examined. The slope of the correlation between the counts in the calcium window and counts in the Te 7 window were calculated. It was determined that the slope of the correlation on the Te standard was approximately 4 (**Figure 3.7**) whereas the slope of the Ca standard was around 30 (**Figure 3.7**). Therefore, it was concluded that samples which displayed a correlation between Ca and Te with a slope greater than 8 could not unequivocally be considered to demonstrate Te instead of Ca counts. On the other hand, if the slope of the correlation between Te and Ca was less than 8, the maps were considered to display Te as opposed to Ca. In samples with low concentrations of Te, it was impossible to differentiate Te from peak overlaps. The only samples where it was possible to differentiate Te from Ca were those with Te concentrations equal to or greater than Ca, per ICP-MS results. The maps that were



determined to display Te with a high degree of confidence were the raw and pressed slimes and the doré furnace soda slag.

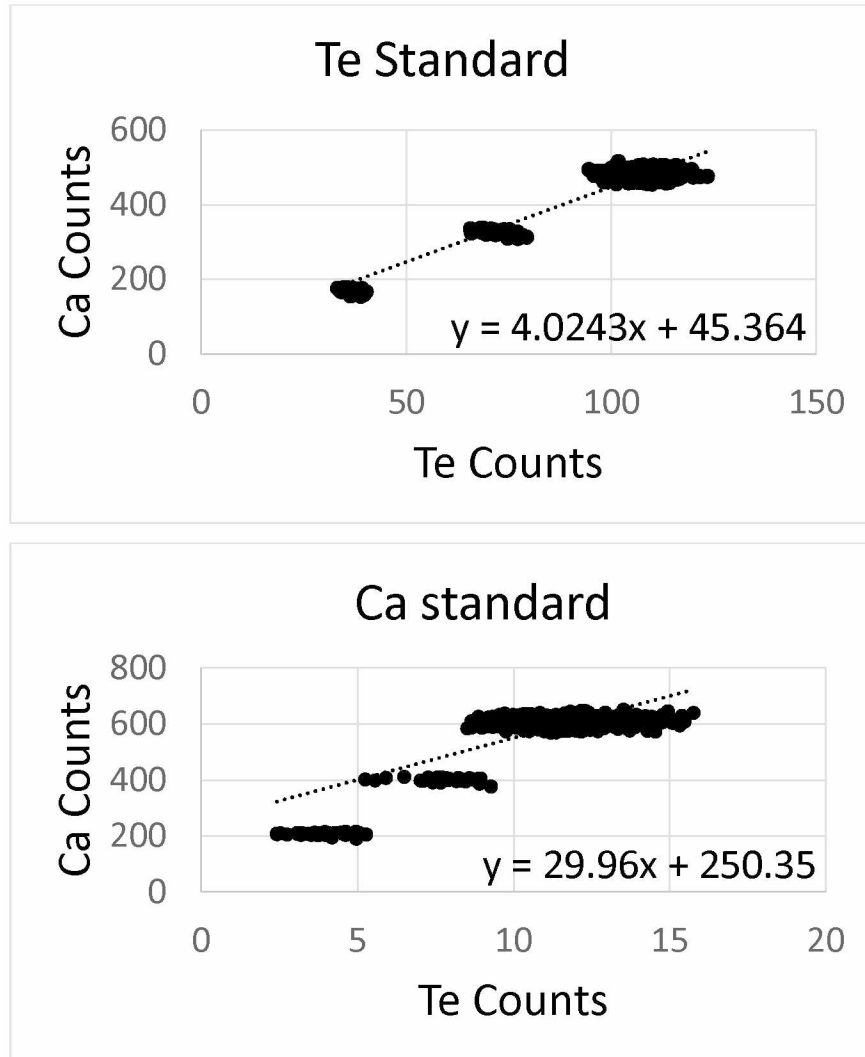


**Figure 3.7** Te counts vs. Ca counts in Te and Ca XRF standards. The top graph shows the correlation between Ca and Te in the Te standard, showing a slope of 4. The bottom graph shows the correlation between Ca and Te in a Ca standard, showing a slope of 30

Map analysis was performed using Sam's Microprobe Analysis Kit (SMAK) (version 1.3) [72]. All maps are normalized for 0 – 100 counts Te, 0 – 1700 counts Ca, 0 – 70 counts S, and 0 – 2000 counts Fe.

### *3.6 Electron Microprobe Analysis*

Electron microprobe analysis (EMPA) has been widely used to analyze environmental samples since the 1960s. Like other micro-focused chemical analysis techniques, the microprobe can be used to determine the elemental composition of areas as small as a few micrometers in diameter. This means that electron probe microanalysis is capable of determining the chemical composition of a single grain and the concentration variations within a single grain. Electron probe microanalysis is typically conducted on polished thin sections that have been coated with a conducting layer to prevent charging of the sample during analysis. The thin sections must be polished because a polished surface prevents the weakening of x-rays often observed in surface scratches and other surface abnormalities.

There are several key components to the EMPA (**Figure 3.8**). The instrument has an electron gun and column, which serves to generate and focus the electron beam. There is also a sample stage and optical microscope; these parts are needed to view and set up the area for analysis. To detect the emissions and intensity of characteristic x-rays needed for chemical analysis, the microprobe has an x-ray detector. The spectrometer can be either wavelength or energy dispersive and, in most cases, an instrument will be set up with both types of detectors. Electron microprobes require high vacuum to maintain prolong the life of the filament and prevent the attenuation of electrons in the column and low energy fluorescent x-rays (such as those from sodium). The imaging display generates and displays an image of the sample as created by backscattered electrons or secondary electron emissions. The image allows for the user to visually distinguish different grains based on their relative atomic weight due to brightness contrast (brighter grains contain higher Z elements).

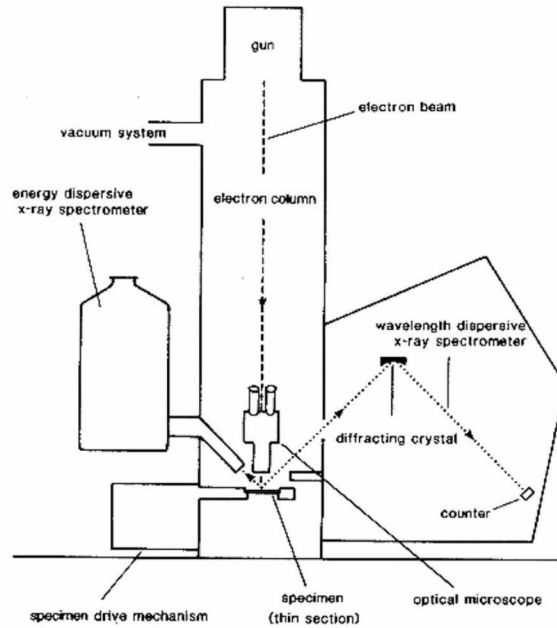


**Figure 3.8** Instrument schematic of a typical microprobe [62].

The interaction between the sample and the microprobe are extremely important to this type of analysis because these interactions determine the capabilities and limitations of the analysis. The volume of interaction is in the magnitude of  $\mu\text{m}^3$  and is known as the excited volume and represents the region in which analytical signals originate. There are multiple phenomena that can happen when the electron beam hits the sample. The majority of electrons will enter the sample and collide with the atoms in the sample. Most of these electrons will lose their energy via collision and heat transfer and come to rest. Some of the electrons will have collisions so strong that they will scatter back out of the sample. These electrons will generate the backscatter electron signal, which can be used to give qualitative compositional data on the sample because phases with higher mean atomic number will appear brighter. Some electrons will go on to ionize the atoms of the sample. This will generate the secondary electron image, which can be used to study sample morphology.

The interaction between the electron beam and the sample can also lead to the emission of x-rays. The two main types of x-rays produced are continuum x-rays and characteristic x-rays. Continuum x-rays are produced when the electron beam interacts with the outer electrons in the sample. The electric field created by these electrons will result in the

emission of a continuous x-ray spectrum, also referred to as the bremsstrahlung. Characteristic x-rays are produced when the electron beam ejects or excites an inner electron. As the unstable excited electron rapidly rearranges itself, energy in the form of an x-ray is released. Since these x-rays are characteristic to the element, they are used in both qualitative and quantitative elemental analysis. Because of the high intensity of the continuum x-rays produced simultaneously with the characteristic x-rays the usual detection limit of chemical analysis by a microprobe is  $500 \text{ mg}\cdot\text{kg}^{-1}$  as opposed to the  $1\text{-}10 \text{ mg}\cdot\text{kg}^{-1}$  often seen with XRF analysis.

When using the microprobe to do an elemental analysis, there are two types of spectrometers—wavelength dispersive spectrometer (WDS) and energy dispersive spectrometer (EDS). For this project, EDS was used. Energy dispersive spectrometers are useful because of their ability to perform rapid qualitative analysis, much faster than their WDS counterparts. Also, EDS can be positioned much closer to the sample than WDS. This allows for EDS to detect a much wider range of x-ray energies than WDS. Another advantage to EDS is that their calibrations are generally much more stable than WDS. This is mainly because their spectrometer response is more reproducible, which allows for a “once and for all” calibration under present condition rather than the need to keep recalibrating. However, WDS is much more accurate and offers lower limits of detection than EDS [62].

### *3.6.1 Experimental Conditions*

The JEOL JXA-8530F Electron Microprobe housed in UAFs’ AIL was used for all microprobe analysis. The electron beam voltage was set of 20 keV and the selected grains were analyzed for 100 seconds. The microprobe was equipped with a Thermo System 7 SDD-EDS system, and Thermo-NSS software (version 3.2) was used for analysis. In particular, the feature sizing option of the Thermo-NSS software was used to help identify Te-bearing grains. Because Te-bearing grains have a higher than average mean atomic weight, the software was set to identify and analyze grains with higher brightness than chalcopyrite on the backscattered electron image. This feature made it much easier and faster to find Te-bearing grains.



## Chapter 4 Results

### 4.1 Method Development and Verification

A sodium peroxide ( $\text{Na}_2\text{O}_2$ ) sinter method was developed to dissolve samples prior to ICP-MS analysis of elemental composition. Prior to analysis of samples, replicate analyses of this method were performed on two matrix-matched standard reference materials NIST 2780 Hard Rock Mine Waste and the Natural Resources Canada, CCU-1d, a copper mine concentrate. **Tables 4.1 and 4.2** display the results, as well as, the relative standard deviation (%RDS), range, and percent difference from the reported values (calculated using **Equation 4.1**).

$$\% \text{ difference} = \frac{|\text{average value} - \text{reported value}|}{\text{reported value}} \times 100 \quad \text{Equation 4.1}$$

For both SRM, the measured Te values were within the standard deviation error of the reported value.

**Table 4.1** NIST 2780 standard reference material analysis by the standard addition ICP-MS method. Accuracy and precision of measurements based on measurements from 10 replicate samples.

Element:	Average (ppm):	%RSD	Range:	Reported NIST value (ppm):	Percent Difference:
Ca	18000 ± 1000	5.6%	16000 – 19000	1950 ± 200	798%
Ti	6200 ± 800	13%	4900 – 7100	6990 ± 190	12%
V	260 ± 30	12%	240 – 320	268 ± 13	3%
Cr	41 ± 4	9.6%	35 – 45	44*	8%
Mn	490 ± 40	8.2%	410 – 560	462 ± 21	5%
Zn	3400 ± 800	24%	2600 – 4100	2570 ± 160	33%
As	52 ± 5	9.6%	46 – 62	48.8 ± 3.3	7%
Se	7 ± 1	14%	6 – 8	5*	43%
Ag	29 ± 6	21%	25 – 44	27*	9%
Cd	11 ± 1	9.1%	9.0 – 13	12.1 ± 0.24	5%
Te	5 ± 1	20%	2 – 5	5*	8%
Au	0.45 ± 0.09	20%	0.33 – 0.65	0.18*	148%
Pb	5800 ± 600	10%	4800 – 7000	5770 ± 410	1%

\*values are reported by NIST for informational purposes only

**Table 4.2** CCU-1d standard reference material analysis by the standard addition ICP-MS method. Accuracy and precision of measurements based on measurements from 9 replicate samples.

Element:	Average (ppm):	%RSD	Range:	Reported CCU-1d value (ppm):	Percent Difference:
Ca	5000 ± 1000	24%	3000 – 6000	1950 ± 210	143%
Ti	80 ± 20	22%	100 – 50	66 ± 7.5*	28%
Mn	90 ± 20	23%	50 – 120	99.4 ± 7.9	10%
Ni	5.7 ± 0.5	7%	5 – 7	7.6 ± 1.6*	29%
Zn	23000 ± 5000	22%	12000 – 27000	26300 ± 1200	2%
As	500 ± 100	29%	400 – 800	545 ± 48*	10%
Se	260 ± 80	9%	100 – 410	244 ± 37*	10%
Ag	110 ± 20	17%	60 – 130	120.7 ± 3.8	8%
Cd	300 ± 100	47%	200 – 700	245 ± 17.3	41%
Te	39 ± 3	7%	36 – 45	36.7 ± 7.4*	6%
Au	3 ± 2	75%	1 – 7	14.01 ± 0.34	81%
Ba	2.6 ± 0.6	25%	1 – 4	12.41 ± 0.82*	79%
Pb	2400 ± 300	14%	1500 – 2500	2620 ± 15	10%

\*values are reported by Natural Resources Canada as provisional due to high inter-laboratory variability.

Calcium was a major containment, which is common in ICP-MS analysis [73]. Gold also was inaccurate for both standards, but for NIST 2780 the concentration was higher than the reported value and for CCU-1d it was lower than the reported value. The concentration determined for Zn was much higher than reported for NIST 2780, but was within two percent for CCU-1d. Zinc is commonly found in lab gloves, which could explain the higher reported value. Another problematic element was Ba, which gave significantly lower values than the reported values in CCU-1d, potentially indicating precipitation of BaSO<sub>4</sub>, a highly insoluble salt ( $k_{sp}=1.1 \times 10^{-10}$ ).

#### 4.2 Elemental Analysis of Samples

Elemental analysis was performed by ICP-MS on samples from the ASARCO mine, smelter and refinery (**Table 4.3**). It was found that the slimes and samples from the refinery are about 1000x more concentrated in Te and Se than the mine and smelter samples. There is substantial variability in the Te concentration of the ore and mine samples: ore samples ranging

**Table 4.3** Inductively coupled plasma mass spectrometry results of mine, smelter and refinery samples based on three replicates reported in  $\text{mg}\cdot\text{kg}^{-1} \pm$  standard deviation

ID #:	Sample:	Te:	Se:	Ag:	Pt:	Bi:	Ba:	Pb:
<b>Ore Samples</b>								
342	Argillite blast	$0.81 \pm 0.07$	$5 \pm 1$	$5.3 \pm 0.4$	$0.13 \pm 0.01$	$11 \pm 1$	$200 \pm 40$	$78 \pm 2$
343	Diposide blast	$1.06 \pm 0.04$	$6 \pm 1$	$4.8 \pm 0.3$	$0.14 \pm 0.01$	$11 \pm 1$	$8.6 \pm 0.2$	$230 \pm 30$
344	Diposide blast	$4.6 \pm 0.9$	$7.7 \pm 0.9$	$9.5 \pm 0.6$	$0.11 \pm 0.03$	$22 \pm 8$	$4.7 \pm 0.4$	$70 \pm 10$
345	Garnet blast	$12 \pm 2$	$21 \pm 6$	$53 \pm 5$	$0.13 \pm 0.09$	$250 \pm 20$	$5.0 \pm 0.7$	$3,000 \pm 300$
348	Red Hill Pit	$4 \pm 1$	$63 \pm 4$	$13 \pm 3$	$0.073 \pm 0.01$	$18 \pm 4$	$28 \pm 2$	$80 \pm 20$
<b>Mine Samples</b>								
346	N. Mission concentrate	$10 \pm 1$	$58 \pm 6$	$87 \pm 5$	$0.3 \pm 0.2$	$250 \pm 30$	$23 \pm 2$	$1,600 \pm 100$
347	S. Mission concentrate	$4.9 \pm 0.3$	$62 \pm 6$	$110 \pm 20$	$0.14 \pm 0.03$	$270 \pm 30$	$12 \pm 2$	$1,600 \pm 200$
352	Ray Mine concentrate	$12 \pm 2$	$139 \pm 9$	$79 \pm 3$	$0.5 \pm 0.1$	$16 \pm 1$	$15.0 \pm 0.7$	$520 \pm 10$
416	N. Mission flotation head	$3 \pm 1$	$30 \pm 15$	$19 \pm 1$	$0.13 \pm 0.04$	$17 \pm 5$	$120 \pm 7$	$164.5 \pm 0.1$
417	N. Mission flotation tail	$1.9 \pm 0.8$	$18 \pm 8$	$13.7 \pm 0.4$	$0.12 \pm 0.04$	$8 \pm 1$	$120 \pm 10$	$190 \pm 30$
418	N. Mission concentrate	$15 \pm 1$	$93 \pm 2$	$220 \pm 10$	$0.4 \pm 0.2$	$910 \pm 20$	$9.8 \pm 0.5$	$8,200 \pm 200$
<b>Smelter Samples</b>								
351	Flash furnace dust	$158 \pm 6$	$400 \pm 26$	$221 \pm 5$	$0.31 \pm 0.04$	$32,000 \pm 1000$	$80 \pm 10$	$43,000 \pm 2000$
353	Convertor dust	$30 \pm 2$	$141 \pm 5$	$180 \pm 11$	$0.18 \pm 0.3$	$2,500 \pm 200$	$71 \pm 5$	$4,700 \pm 400$
467	Flash furnace slag	$1.3 \pm 0.4$	$17 \pm 3$	$15 \pm 1$	$0.25 \pm 0.03$	$27.3 \pm 0.3$	$50 \pm 1$	$2,100 \pm 300$
<b>Refinery Samples</b>								
349	Doré soda slag	$5,700 \pm 200$	$7,600 \pm 400$	$6,000 \pm 700$		$23,000 \pm 4000$	$55,000 \pm 5000$	$24,000 \pm 1000$
350	Doré dust	$5,800 \pm 200$	$32,000 \pm 1000$	$2,900 \pm 400$	$2.2 \pm 0.1$	$5,600 \pm 200$	$2,320 \pm 40$	$3,000 \pm 100$
354	Raw slimes	$24,000 \pm 1000$	$193,900 \pm 7000$	$7,600 \pm 400$	$8 \pm 1$	$17,000 \pm 1000$	$16,400 \pm 300$	$10,700 \pm 800$
355	Pressed slimes	$27,000 \pm 1000$	$130,000 \pm 30000$	$1,900 \pm 300$	$4.4 \pm 0.5$	$10,000 \pm 1000$	$6,600 \pm 400$	$6,900 \pm 100$



from 0.81 to 4.6 mg·kg<sup>-1</sup> Te and the copper concentrates contained 4.9 to 15 mg·kg<sup>-1</sup> Te. Waste products from the smelter contained 1.3 mg·kg<sup>-1</sup> Te in the slag, indicating that Te does not substantially partition into the slag phase, and 30 to 158 mg·kg<sup>-1</sup> Te in the smelter dusts, pointing to substantial volatilization of Te during smelting. At the refinery, waste products from the doré furnace contained 5,700 to 5,800 mg·kg<sup>-1</sup> Te. This elemental analysis was used to calculate the mass balance of Te, and constrain XAS fits used to probe Te and S speciation.

Bulk XRF analysis was used to perform quantitative elemental analysis of copper concentrates, pyrite and chalcopyrite separates, and a chalcopyrite slab taken from mine ores (**Table 4.4**). The Te concentrations were at 12 to 11 mg·kg<sup>-1</sup> Te in the two pyrite separates yielded and 2 ± 1 to 7 ± 3 mg·kg<sup>-1</sup> Te in chalcopyrite separates (**Table 4.4**). The copper concentrates yielded concentrations of 12 – 28 mg·kg<sup>-1</sup> Te, higher than the 5 – 12 mg·kg<sup>-1</sup> Te found using ICP-MS. Sulfide mineral separate Te concentrations were lower than the Te concentrations measured in the copper concentrates, indicating the presence of a minor, high Te phase, likely telluride minerals.

It has been noted that there seems to be a difference between the concentrations reported by ICP-MS and XRF, with XRF results being significantly greater than those reported by ICP-MS (**Tables 4.3 and 4.4**). This is most likely caused by incomplete dissolution of the samples or mineral precipitation from solution prior to ICP-MS analysis. However, it should be noted that there was no visible incomplete dissolution. Another possible source of higher XRF values is the concentrations are sufficiently close to the XRF detection limit that the quoted uncertainties (1 standard deviation of the mean value based on at least 6 measurements) are likely much greater.

#### *4.3 Mass Balance*

In order to better understand Te behavior during the Cu extraction process, the mass balance of Te was calculated for the mining and smelting processes, which was calculated using exclusively ICP-MS results (**Figure 4.1**). This is in part because some of the samples were below the lower limit of detection of 3 mg·kg<sup>-1</sup> for Te for bulk WD-XRF. The ore and blast hole samples at Mission Mine contained 0.81 ± 0.07 to 4.6 ± 0.9 mg·kg<sup>-1</sup> Te (**Table 4.3**). In the mass balance

**Table 4.4** X-ray fluorescence results from concentrate samples and pyrite and chalcopyrite ore separates reported in  $\pm$  standard deviation

#:	Sample:	Cu:	Fe:	S:	Te:	Se:	Ag:	Bi:	Pb:	Sb:
		%	%	%	mg·kg <sup>-1</sup>	mg·kg <sup>-1</sup>	mg·kg <sup>-1</sup>	mg·kg <sup>-1</sup>	mg·kg <sup>-1</sup>	mg·kg <sup>-1</sup>
346	N. Mission concentrate	19.6 $\pm$ 0.1	28.1 $\pm$ 0.12	35.8 $\pm$ 0.16	13 $\pm$ 3	64 $\pm$ 2	112 $\pm$ 4	200 $\pm$ 5	1740 $\pm$ 9	112 $\pm$ 3
347	S. Mission concentrate	30.8 $\pm$ 0	26.9 $\pm$ 0.4	33.8 $\pm$ 0.2	12 $\pm$ 1	88 $\pm$ 0	149 $\pm$ 5	271 $\pm$ 2	1970 $\pm$ 30	163 $\pm$ 3
352	Ray Mine concentrate	23.5 $\pm$ 0.14	27.8 $\pm$ 0.1	32.5 $\pm$ 0.9	27 $\pm$ 2	154 $\pm$ 2	99 $\pm$ 1	14 $\pm$ 1	571 $\pm$ 9	63 $\pm$ 1
418	N. Mission concentrate	25.3 $\pm$ 0.2	26.4 $\pm$ 0.1	33.7 $\pm$ 0.1	28 $\pm$ 7	126 $\pm$ 2	230 $\pm$ 10	905 $\pm$ 13	9800 $\pm$ 200	81 $\pm$ 7
338-Py	Pyrite Separate 1	1.38	37.4	44.0	12	32	-		89	-
338-Py	Pyrite Separate 2	0.077	28.9	33.9	11	48	-	-	165	-
	Chalcopyrite Slab from Reichardt	30.6 $\pm$ 0.1	28.1 $\pm$ 0.1	35.1 $\pm$ 0.1	2 $\pm$ 1	39 $\pm$ 2	91 $\pm$ 4	9 $\pm$ 2	63 $\pm$ 3	4 $\pm$ 4
335-Cp	Chalcopyrite Separate 1	32.7	28.08	32.8	7 $\pm$ 5	-	0.007	-	-	-
335-Cp	Chalcopyrite Separate 2	29.7	25.4	29.7	7 $\pm$ 3	0	0.01	-	0.01	-

calculation, flux numbers were provided by ASARCO for April, 2012 and Te concentrations were measured in samples collected during a synoptic sampling of the North Mission Mine. The flotation feed, mine tailings, and Cu concentrate samples contained  $3 \pm 1 \text{ mg}\cdot\text{kg}^{-1}$ ,  $1.9 \pm 0.8 \text{ mg}\cdot\text{kg}^{-1}$ , and  $15 \pm 1 \text{ mg}\cdot\text{kg}^{-1}$ , respectively (**Table 4.3**). These values are perhaps high for the ore, but contain similar Te values to other concentrates measured ( $4.9$  to  $12 \text{ mg}\cdot\text{kg}^{-1}$  Te). The results indicate that  $11 \pm 1\%$  of Te is present in the Cu concentrate destined for additional processing at the smelter, while  $60 \pm 30\%$  of the Te reports to the fine-grained mine tailings released into the surficial environment. The large error associated with the measured concentration of Te in the ore and mine tailings, due to heterogeneity of ore and low concentrations of Te, are the largest source of error in the overall mass balance calculation.

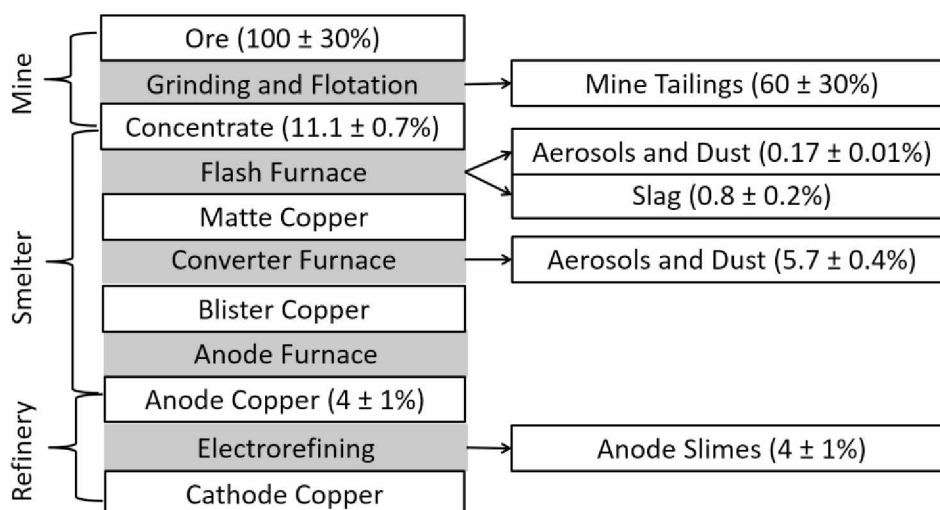


**Figure 4.1** Mass balance of Te during the mining and smelting process. Values shown include one standard deviation of analytical error, which is a very low estimate of the true error associated with these values.

At the smelter the Cu concentrate is heated sequentially in the flash, converter, and anode furnaces. In the flash furnace,  $\text{SiO}_2$  and oxygen are added to the concentrate, producing two waste products:  $\text{SO}_2$  (g), the dusts from which contain  $158 \pm 6 \text{ mg}\cdot\text{kg}^{-1}$  Te, and slag, which contains  $1.3 \pm 0.4 \text{ mg}\cdot\text{kg}^{-1}$  Te. In the flash furnace, 1.0% of the Te is lost— $0.17 \pm 0.01\%$  to gas cleaning and  $0.8 \pm 0.2\%$  to the slag. The converter furnace also produces  $\text{SO}_2$  (g) the dusts from which contain  $30 \pm 2 \text{ mg}\cdot\text{kg}^{-1}$  Te, representing  $5.7 \pm 0.4\%$  of the total Te. The blister copper is

then passed through an anode furnace and poured into anode molds. The copper anodes contain  $4 \pm 1\%$  of the Te originally present in the ore.

At the refinery, 99% Cu anodes are electrorefined to produce 99.9% Cu cathodes for industrial application. Nearly all impurity elements present in Cu anodes report to the anode slimes, which are further processed to remove Au, Ag, Pt group elements, Se, and Te [23]. Tellurium is produced as a byproduct from the  $\text{CuSO}_4$  removed during autoclaving and from the doré furnace soda slag [48, 49]. The concentration of Te in the raw slimes and pressed slimes is  $2.4 \pm 0.1\%$  Te and  $2.7 \pm 0.1\%$  Te respectively. The ASARCO refinery reports 60% recovery of Te from the raw anode slimes. Taking this into account, only  $2.4 \pm 0.6\%$  of Te present in the original Cu ore is recovered as a byproduct and available for industrial applications.

#### *4.4 X-Ray Absorption Spectroscopy*

X-Ray absorption spectroscopy (XAS) was used to determine the speciation of S and Te in samples with sufficiently high concentrations, estimated at  $\sim 100 \text{ mg kg}^{-1}$  for Te K-edge. Sulfur and Te are both group 16 elements and, thus, have the same possible oxidation states. Examination of S, which is expected to be present at much higher mass fractions in all samples than Te, is expected to lend insight into Te behavior. Analyzing how the speciation of S and Te changes during Cu ore processing will give insight into the behavior of Te.

##### *4.4.1 Sulfur*

Sulfur XAS spectra were collected for the furnace dust, convertor dust, raw slimes, pressed slimes, and the doré furnace soda slag. These samples were selected for this analysis because it was believed that their S speciation could lend insight into the speciation and behavior of Te. The two dust filters from the furnace and converter contain mainly reduced forms of S as troilite ( $\text{FeS}$ ), chalcocite ( $\text{Cu}_2\text{S}$ ), and pyrite ( $\text{FeS}_2$ ) (converter dust only) with minor amounts of S present as sulfate, using goslarite ( $\text{ZnSO}_4 \cdot 7\text{H}_2\text{O}$ ) as a model, (**Figure 4.2; Table 4.5**). The S speciation of the slimes shows that they contain mostly oxidized S, using barite ( $\text{BaSO}_4$ ) and chalcantite ( $\text{CuSO}_4 \cdot 5\text{H}_2\text{O}$ ) to model  $\text{SO}_4^{6+}$ , with minor amounts of reduced S, using as chalcocite as a model (**Figure 4.3; Table 4.5**). The Amarillo Refinery soda slag from the doré

furnace is mostly oxidized S in the form of barite and goslarite (**Figure 4.3; Table 4.5**). These phases may or may not be present in the sample and were used to represent either oxidized or reduced sulfur minerals. The goal of this analysis was to quantify the fraction of oxidized sulfur species rather than identify specific phases. Unsurprisingly, the results indicate progressive oxidation throughout the smelting and refining process.

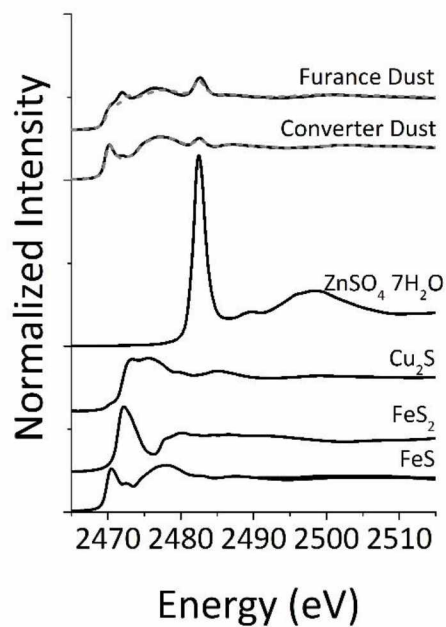


**Figure 4.2** S XAS of furnace dust (sample 351) and converter dust (sample 353) from the Hayden Smelter. Data is shown as a black solid line and fit is shown as a gray dashed line.

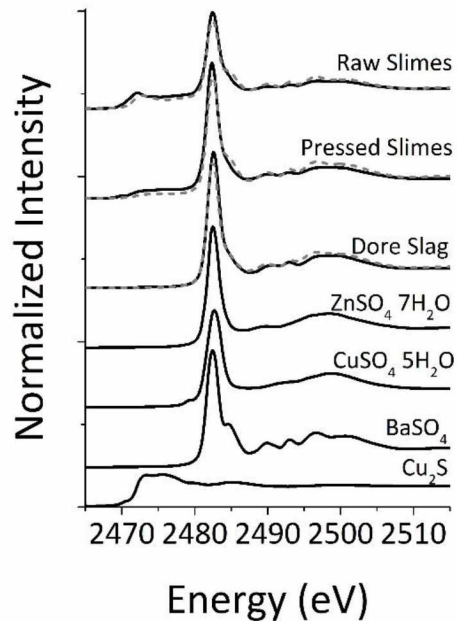


**Figure 4.3** S XAS of the raw anode slimes (sample 354), pressed anode slimes (sample 355), and doré furnace soda slag (sample 349) from the Amarillo Refinery. Data is shown as a black solid line and fit is shown as a gray dashed line.

**Table 4.5** Linear combination fits results for S XAS. Results shown in percentages.

#	Sample	FeS	Cu <sub>2</sub> S	FeS <sub>2</sub>	BaSO <sub>4</sub>	CuSO <sub>4</sub> ·5H <sub>2</sub> O	ZnSO <sub>4</sub> ·7H <sub>2</sub> O	Sum	χ <sup>2</sup>	Red. X <sup>2</sup>
351	Furnace Dust	53	25	12			9	99	2.56	2.6 x 10 <sup>-3</sup>
353	Convertor Dust	56	32				9	97	3.41	2.4 x 10 <sup>-3</sup>
354	Raw Slimes		35		61	10		106	20.0	2.0 x 10 <sup>-2</sup>
355	Pressed Slimes		12		74		28	114	44.3	4.4 x 10 <sup>-2</sup>
349	Doré Soda Slag				49		60	109	17.8	1.8 x 10 <sup>-2</sup>

#### 4.4.2 Tellurium

Linear combination fits of XAS were performed to qualitatively assess the ratio of oxidized and reduced tellurium. Again, the goal is to examine the ratio of oxidized and reduced species of Te rather than identify specific phases. Analyses were performed on the flash furnace filter, raw anode slimes, pressed anode slimes, the doré furnace soda slag and the doré furnace filter. These samples were analyzed because their concentration of Te was above the estimated detection limit, estimated at 100 mg·kg<sup>-1</sup>, under the XAS collection conditions. Here fits were performed using sodium tellurate, sodium tellurite, and paratellurite as model

compounds for oxidized Te and tellurides including calaverite ( $\text{AuTe}_2$ ) and  $\text{Bi}_2\text{Te}_3$  as models for reduced Te species. Complicating this analysis is the fact that data was collected at two different vertical slit sizes (0.5 and 2 mm), complicating the fitting for each spectra. However, only references collected at the same slit size were used in fitting each sample spectra.

Linear combination fits of the flash furnace dust filter 53% of the Te is oxidized while 49% is reduced (**Figure 4.4; Table 4.6**). In the raw slimes, 49% of the Te is reduced and 51% is oxidized. The results are similar for the pressed slimes (**Figure 4.5; Table 4.6**). The Te in the soda slag from the Doré furnace is 43% reduced and 57% oxidized when modeled with  $\text{Na}_2\text{TeO}_3$  and 74% reduced and 27% oxidized when modeled with  $\text{Na}_2\text{TeO}_4$ . The dust filter is 25% reduced and 76% oxidized (**Figure 4.5; Table 4.6**). These results indicate progressive Te oxidation throughout the process.

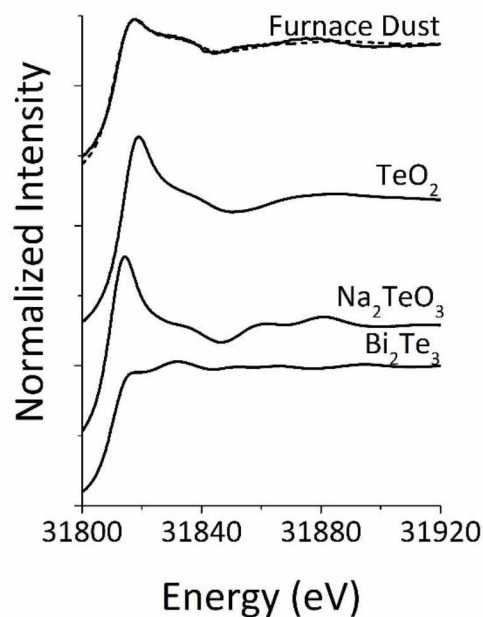


**Figure 4.4** Te XAS of the flash furnace dust (sample 351) from the Hayden Smelter. Data is shown as a black solid line and fit is shown as a gray dashed line. This sample was collected with 0.5 mm slits.

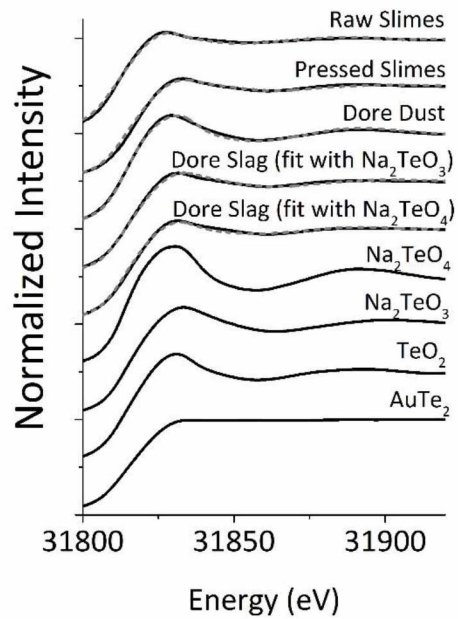


**Figure 4.5** Te XAS of the raw anode slimes (sample 354), pressed anode slimes (sample 355), doré furnace dust (sample 350), and doré furnace soda slag (sample 349) from the Amarillo Refinery. The doré furnace soda slag was fit with both tellurite and tellurate. Data is shown as a black solid line and fit is shown as a gray dashed line.



**Table 4.6** Linear combination fits results for Te XAS. Results shown in percentages.

#:	Sample Description:	BiTe:	AuTe <sub>2</sub> :	TeO <sub>2</sub> :	Na <sub>2</sub> TeO <sub>3</sub> :	Na <sub>2</sub> TeO <sub>4</sub> :	Sum:	$\chi^2$ :	Red. $\chi^2$ :
354	Raw Slimes		49	51			100	0.17	$7.2 \times 10^{-5}$
355	Pressed Slimes		57		43		100	0.69	$2.9 \times 10^{-4}$
351	Flash Furnace Filter	57			44		101	2.46	$9.5 \times 10^{-4}$
349	Doré Furnace Slag		43		57		100	0.45	$1.8 \times 10^{-4}$
349	Doré Furnace Slag		74			27	101	0.39	$1.6 \times 10^{-4}$
350	Doré Furnace Filter		42			60	102	0.43	$1.8 \times 10^{-4}$

These Te models are more representative of tellurium oxidation state, oxidized vs reduced tellurium, rather than indicative of specific phases present. In many cases the minerals identified by electron microscopy were not present in the Te XAS reference library. This is likely to increase the error associated with these fits above the generally accepted 10% [74]. Sensitivity testing was performed by varying the identity of model compounds used to represent oxidized, and to a lesser extent reduced, species in the fits after a good fit had been achieved. In most cases, the identity of the fit components can be considered unique because switching the identity of the oxidized model compound resulted in substantial reduction in the statistical goodness of fit (indicated by reduced  $\chi^2$  values). However, in one case doré filter soda slag (sample 349), sodium tellurate and sodium tellurite fits returned similar chi-squared statistics (**Figure 4.4, Table 4.6**). Nonetheless, Te XAS are a useful tool in estimating the fraction of oxidized Te in these samples.

#### *4.5 Micro-focused X-Ray Maps*

Micro-focused XRF maps were collected to determine which elements spatially collocate with Te. Due to potential energy overlaps between Ca and Te (**Table 3.6**), not every sample could be unambiguously deconvoluted to show the spatial distribution of Te with a high degree of certainty (section 3.5.2). The three samples that definitively mapped Te to a high degree of confidence are the raw and pressed anode slimes and the doré furnace soda slag. For all other samples it was hard to distinguish between Te and Ca. All three samples showed a collocation between Te and S. The raw slimes showed the highest degree of correlation with an  $R^2$  value of 0.96 (**Figure 4.6**). The pressed slimes also showed a high degree of correlation between Te and S with  $R^2=0.85$  (**Figure 4.6**). Again in the refinery soda slag there was a correlation between Te and S, but not as strong as seen in the slimes ( $R^2=0.50$ ) (**Figure 4.6**). In the refinery soda slag, several different populations are evident, indicating distinct stoichiometric relationships between S and Te. Distinct from the highly correlated Te-S population, there is a subset of points with high Te and low S, potentially indicating the presence of a telluride phase. There were no other elements measured that statistically correlated with Te in any sample.

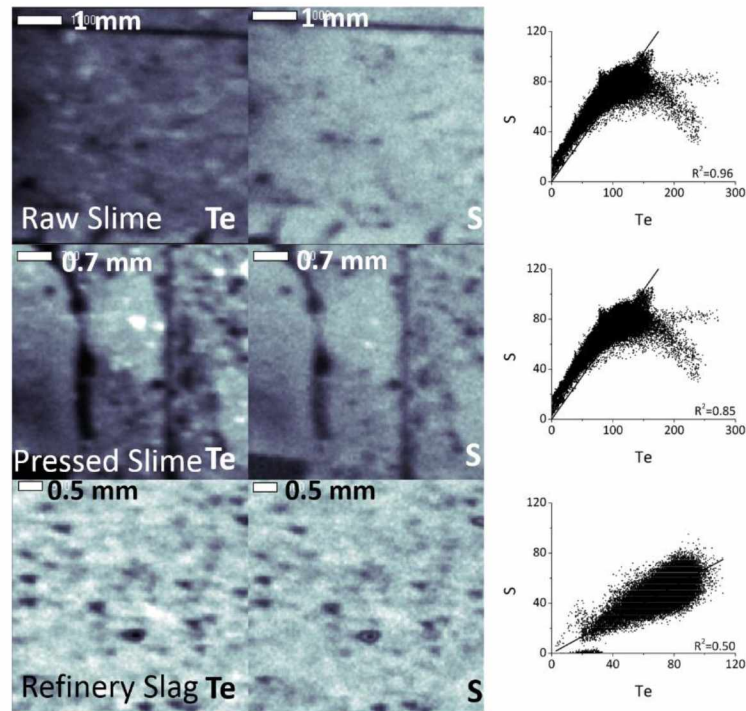


**Figure 4.6** X-ray fluorescence maps showing the correlation between Te and S in the raw anode slimes, pressed anode slimes, and refinery soda slag. All three samples, display a strong collocation between S and Te.

#### 4.6 Electron Microprobe Analysis

Electron microscopy was used to determine the Te bearing phases in the copper concentrate and anode slimes. Microprobe analysis was also applied to the furnace filter and converter filter, the grain size was very small and no Te bearing grains were found. For the Cu concentrate samples (bulk Te concentrations 4.9-15 mg kg<sup>-1</sup>), the microprobe was used to identify the telluride minerals in the concentrate. Microprobe analysis of the copper concentrate found a few concentrated Te-bearing grains identified as telluride minerals (**Figure 4.7**). The minerals found include: altaite (PbTe), likely hessite (Ag<sub>2</sub>Te), cervelleite (Ag<sub>4</sub>TeS), tetradymite (Bi<sub>2</sub>Te<sub>2</sub>S), and Tsumoite (BiTe) (**Figure 4.7; Table 4.7**). The altaite and tsumoite were found occluded in a grain of chalcopyrite, whereas the other minerals were found as individual grains (**Figure 4.7**).

These measurements are complicated due to small particle size and particles are often smaller than the excitation volume of the electron beam. This often results in the excitation of

the target telluride mineral as well as nearby or hosting sulfide phases. Additionally, the overlap of Bi M-line (2,345.5 eV) and the sulfur K-line (2,307.84 eV) can be difficult to deconvolute using an energy dispersive detector, like that used for these analyses. Despite these complications, several Te-bearing phases were identified.

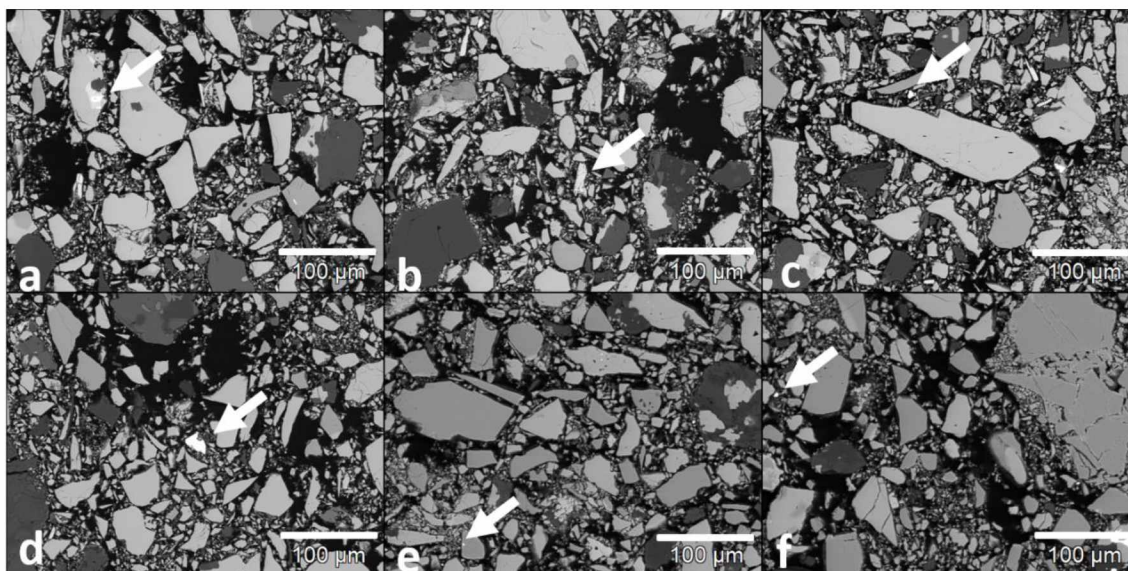


**Figure 4.7** Backscattered electron images of Cu concentrate samples. A) An image of PbTe included in a chalcopyrite grain from the Ray Mine (sample 352). B) A grain of  $\text{Ag}_4\text{TeS}$  also included in a chalcopyrite grain from the Ray Mine (sample 352). C) A grain of  $\text{Ag}_2\text{Te}$  from the Ray Mine (sample 352). D) A grain of  $\text{Bi}_2\text{TeS}$  found in the Ray Mine concentrate (sample 352). E) A grain of BiTe found in the Mission Mine concentrate (sample 346). F) A grain of  $\text{Bi}_2\text{Te}_2\text{S}$  from the Mission Mine (sample 346).

**Table 4.7** The composition by weight percent of the Te-bearing grains in concentrate found with the microprobe.

Grain:	Te:	Ag:	Bi:	Pb:	S:	Measured formula:	Likely formula:	Likely mineral name:
A	40 ± 2			60 ± 1		$\text{PbTe}_{1.1}$	PbTe	Altaite
B	21 ± 3	75 ± 3			5 ± 1	$\text{Ag}_{4.4}\text{Te}_{1.3}\text{S}$	$\text{Ag}_4\text{TeS}$	Cervelleite
C	31 ± 1	69 ± 3				$\text{Ag}_{2.6}\text{Te}$	$\text{Ag}_2\text{Te}$	Hessite
D	33 ± 3		62 ± 4		4 ± 1	$\text{Bi}_{2.4}\text{TeS}$	$\text{Bi}_2\text{TeS}$	Ingodite
E	42 ± 1		58 ± 2			$\text{BiTe}_{1.2}$	BiTe	Tsumoite
F	45 ± 3		50 ± 4		5 ± 1	$\text{Bi}_{1.5}\text{Te}_{2.3}\text{S}$	$\text{Bi}_2\text{Te}_2\text{S}$	Tetradymite

The mineralogy of tellurium in the raw anode slimes is much more complicated. The tellurium phases appear to be complex systems that contains O, S, Ag, As, Sb, Te in different stoichiometric ratios (**Figure 4.8; Table 4.8**). These results are similar to the analysis of copper anode slimes performed by Chen (1996), in which the authors identified 90+% as a telluride, ~5% as the oxidate phase and <5% remains in the electrolyte [47].

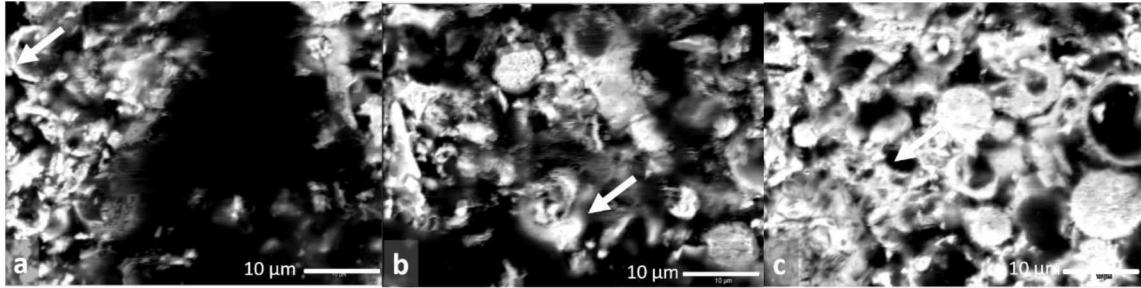


**Figure 4.8** Backscattered electron images of the raw slimes

**Table 4.8** The composition by weight percent of Te-bearing grains found in anode slimes (sample 354).

Grain:	Ag:	Cu:	Pb:	S:	As:	Se:	Sb:	Te:	O:	Formula:
A	39 ± 1					48 ± 2		13 ± 1		Ag(Se,Te) <sub>2</sub>
B	23 ± 1	5 ± 1	26 ± 2	5 ± 1	20 ± 1	28 ± 1	8 ± 1	13 ± 1	8 ± 1	oxidate phase [47]
C	23 ± 1	9 ± 1	1 ± 1	8 ± 1	6 ± 2	30 ± 1	12 ± 1	11 ± 1	18 ± 7	oxidate phase [47]

## Chapter 5 Discussion

Concerns of Te scarcity combine with industrial demand for Te has prompted this study to examine Te behavior and speciation during copper ore processing at ASARCO, the only domestic producer of Te, and identify potential methods of optimizing Te recovery. The mass balance of Te throughout the Cu extraction, smelting and refining process was calculated using Te concentrations obtained from peroxide sinter digestion of solid samples followed by elemental analysis by ICP-MS using a standard addition method. Tellurium speciation and mineralogy were directly probed using XAS and EMPA in an effort to connect Te behavior in extraction circuits with mineralogical changes.

### 5.1 Mass Balance

The mass balance of Te at the mine and smelter lends insight into where Te concentrates and is lost during Cu extraction and possible processes or waste products to target in order to optimize Te extraction. Currently, only  $4 \pm 1\%$  of the Te in the ore remains the anode slimes, which are processed for Te extraction and purification (**Figure 4.1**). The majority of Te is lost during the concentration of Cu-bearing minerals at the mine where  $60 \pm 30\%$  of it reports to the mine tailings during the initial milling and concentration process. The tailings deposited into the surficial environment contain  $1.9 \pm 0.8 \text{ mg}\cdot\text{kg}^{-1}$ , which is unlikely to ever be economic once the lucrative Cu is removed. The total Te emerging from the concentration process is significantly less than the amount measured in the mill heads. This could be due to heterogeneity of ore, since samples of heads, tails, and concentrate were collected at the same time. The Te concentrations measured are quite low, and have a high relative error associated with them. Another possible confounding factor is the nugget effect. Meaning that if the Te concentration in the ore is due to a small number of Te-rich grains, then a small sub-sample is likely to be not representative of the whole. However, I found only 6 tiny Te-rich grains in my study of the Cu concentrate samples (**Table 4.6**). This small number cannot account for the Te concentration measured ( $15 \text{ mg}\cdot\text{kg}^{-1}$ ) and suggests that the bulk of the Te is not present as individual Te-rich grains

Whatever the source of variability in these measurements, the mill portion of the mass balance is the largest source of error in the entire mass balance calculation. This variability will be perpetuated throughout the remainder of the extraction circuit, and the true variability associated with the downstream measurements is likely substantially larger than the analytical errors reported.

At the smelter, another  $5.8 \pm 0.4\%$  of Te, over half the remaining Te, is lost in the dust that is filtered from the  $\text{SO}_2$  produced in both the flash furnace and the converter,  $0.17 \pm 0.01\%$  and  $5.7 \pm 0.4\%$  of Te, respectively. Even though the dust from the flash furnace represents such a small fraction of the overall Te, at  $158 \pm 6 \text{ mg}\cdot\text{kg}^{-1}$  Te, this is the smelter waste product with the highest concentration of Te found at the smelter, and, therefore, the highest potential future source for Te extraction at the smelter. The dust from the converter at  $30 \pm 2 \text{ mg}\cdot\text{kg}^{-1}$  has much lower concentration of Te but at  $5.7 \pm 0.4\%$  of the Te, might also be a potential target for Te extraction (**Figure 4.1; Table 4.3**), if a Te-extraction circuit were implemented at the smelter. ASARCO has reported that 60% of the Te in the anode slimes is recovered from the raw anode slimes.

Together, these results indicate that only  $2.4 \pm 0.6\%$  of the Te in ore is extracted and purified for industrial use. Although due to uncertainty associated with total Te entering the mill, the overall error associated with the recovery is likely much larger than the analytical error reported. The Te that does not report to the pressed anode slimes will most likely report to the doré furnace soda slag or dust filter. The doré furnace soda slag contains  $5700 \pm 200 \text{ mg}\cdot\text{kg}^{-1}$  Te and the doré dust filter contains  $5800 \pm 200 \text{ mg}\cdot\text{kg}^{-1}$  Te. At most refinery operations the doré furnace soda slag is further processed for Te, but the filter is not [49]. At such high concentrations of Te, the doré furnace dust filter is also a potential source of Te that could be extracted.

The mass balance results are similar to that reported by Ojebuoboh (2008) (**Figure 1.8**) with a few differences [7]. The Russian mine examined by Ojebuoboh reported a 90% loss of Te to the mine tailings, 6.4% Te lost at the smelter, and 1.4% Te lost at the refinery. The Russian smelter loss 3.9% of Te to the  $\text{SO}_2$  gas cleaning step which is less than the 5.29% ASARCO loses in this same process. This is opposite of what is true for the ASARCO slag; the Russian smelter

loses a total of 4.3% Te to the furnace and convertor slag, while ASARCO only loses  $0.8 \pm 0.2\%$  to the furnace slag. The Russian smelter used an older type of furnace known as a reverberatory furnace, which could not reprocess convertor slag and might explain the differences in mass balance. In order to understand how to increase Te recovery, it is important to examine the Te mineralogy throughout the extraction process.

## 5.2 Mine

Tellurium concentrations in hand samples and blast hole cuttings varied between ore types. In the ICP-MS results, it was found that the garnet skarn has  $12 \pm 2 \text{ mg}\cdot\text{kg}^{-1}$  Te. This is significantly higher than the hornfels sample or the two diopside skarn samples, which were  $0.81 \pm 0.07 \text{ mg}\cdot\text{kg}^{-1}$  Te,  $1.06 \pm 0.04 \text{ mg}\cdot\text{kg}^{-1}$  Te, and  $4.6 \pm 0.9 \text{ mg}\cdot\text{kg}^{-1}$  Te respectively (**Table 4.3**). The amount of Te in the concentrate varies from 12 to  $4.9 \text{ mg}\cdot\text{kg}^{-1}$  (**Table 4.3**); the range is most likely related to the type of ore being processed during collection. The analysis of the pyrite and chalcopyrite ore separates showed that Te is slightly more concentrated in pyrite ( $12 - 11 \text{ mg}\cdot\text{kg}^{-1}$ ) than chalcopyrite ( $7 \text{ mg}\cdot\text{kg}^{-1}$ ; **Table 4.4**). Since pyrite mostly reports to the mine tailings, it is not surprising that the majority of the Te is lost in this step.

Only six Te-bearing mineral grains were found on the concentrate thin sections by microprobe analysis, including: altaite, probably hessite, cervelleite, tetradymite, and tsumoite (**Figure 4.7**; **Table 4.7**). Most of these grains were found as individual mineral grains, however both altaite and tsumoite were both found as an inclusion in a chalcopyrite grain. The microprobe analysis showed no evidence of solid solution of Te within chalcopyrite, like one would suppose is possible since it is known that Se will replace S in the chalcopyrite matrix [75]. However, this is entirely due to the detection limits of the microprobe in EDS mode, generally  $3000 \text{ mg kg}^{-1}$ . Further analysis by SIMS or LA-ICP-MS would be required to explore potential substitution of Te for S in sulfides.

## 5.3 Smelter

An examination on the S and Te XAS lends insight into the changing speciation of the S and Te during copper ore processing. Since not all samples had a high enough concentration of



Te to measure its oxidation with XAS, S absorption was also measured to hopefully gain a better understanding of Te behavior. Analysis of the furnace dust shows that S is 9%  $\text{SO}_4^{2+}$ , 12%  $\text{S}_2^{2-}$ , and 78%  $\text{S}^{2-}$ . The converter dust, on the other hand, is 9%  $\text{SO}_4^{2+}$  and 88%  $\text{S}^{2-}$  (**Figure 4.2; Table 4.5**). Since most of the sulfur present in the concentrate is reduced, these results show an increase in the oxidation of solid state S caused by the furnace and possibly the convertor. This is not surprising, since these are both known to be oxidizing environments and produced oxidized gaseous S in the form of  $\text{SO}_4$  (**Equations 1.1 – 1.4**).

The results for Te are similar to those from S, but differ in the ratios of oxidized and reduced species in each sample. Since most naturally occurring minerals are tellurides [2], it is assumed that most of the Te in the concentrate are tellurides [44, 47]. An examination of the XANES of the furnace dust shows the speciation of Te is 52% reduced and 44% oxidized, modeled using sodium tellurite, which has a smaller white line than tellurate and should be considered a maximum estimation of oxidized Te (**Figure 4.4; Table 4.6**). This means that up to half of the Te that reports to the aerosols present in the  $\text{SO}_2$  is oxidized.

Microprobe data of the flash furnace dust and the convertor dust did not reveal any Te-bearing grains, despite the survey of half a thin section. It is, therefore likely that the reason no Te-bearing grains were identified is because the Te is more evenly distributed than in the concentrate and not present as a telluride mineral. It is reasonable that Te is volatilizing in the high temperature environment and then subliming into aerosol particles smaller than the excitation volume of the microprobe. Thus, unequivocal identification of Te-bearing phases, both oxidized and reduced, was not accomplished.

#### *5.4 Refinery*

The raw and pressed anode slimes have high Te concentrations,  $2.4 \pm 0.1\%$  and  $2.7 \pm 0.1\%$  Te by mass, respectively. The amount of Te in ASARCO's pressed slimes is higher than the 1% previously reported in literature [33]. The high residual amount of Te present in the pressed anode slimes indicates that the Te does not completely dissolve during decopperization and autoclaving processes, and will report to the doré furnace soda slag and dust filter.

The XANES of S and Te at the refinery lend insight into the behavior of S and Te during the autoclaving process. Sulfur XAS indicate significant oxidation during autoclaving, as indicated by linear combination fits of the raw anode slimes 71%  $\text{SO}_4^{2-}$  and 35%  $\text{S}^{2-}$ ; whereas, the pressed slimes were 102%  $\text{SO}_4^{2-}$  and 12%  $\text{S}^{2-}$  (**Figure 4.3; Table 4.5**). The XANES of the slag from the doré furnace showed that S was fully oxidized (**Figure 4.4; Table 4.5**). Linear combination fit totals over 100% are likely due to self-absorption of the sulfate white line in some reference spectra, a common problem in sulfur XANES. Despite this issue, the fits qualitatively indicate the increasing fraction of sulfate minerals through the autoclaving and smelting process.

Tellurium XAS indicate similar trend, with progressive oxidation occurring during the refinery processes. Linear combination fits indicate Te in raw slimes are 49%  $\text{Te}^{2-}$  and 51%  $\text{Te}^{4+}$ , and the pressed slimes are 57%  $\text{Te}^{2-}$  and 43%  $\text{Te}^{4+}$  (**Figure 4.5; Table 4.6**). These results are surprising because previous results reported in literature indicate that the raw slimes are mostly reduced forms of Te with minor amounts of oxidized Te [47]. One possible explanation for the difference is the large vertical slit size used while collecting the data for the raw and pressed slimes. The larger slit size cause the beam to be less intense, making it difficult to characterize unique near edge features on the reference spectra and samples. The Te results do show a different rate of oxidation than S. Sulfur in the pressed slimes is fully oxidized to  $\text{SO}_4^{2-}$ , while Te is a combination of  $\text{Te}^0$  and  $\text{Te}^{4+}$  with no matches to  $\text{TeO}_4^{2-}$  species found. This is different from the doré furnace samples, which show that S is more oxidized than Te.

Grain-scale mineral identification was performed using electron microscopy and micro-focused XRF. The XRF maps done at SSRL show that Te and S are collocated in the raw slimes, pressed slimes, and the doré furnace slag (**Figure 4.6**). There was no definitive evidence of Te being collocated with Ag, Au, Bi, or Pb. Whatever mineralogical form that Te as in initially, it has certainly changed by the time the ore has gone through all the various processing steps. The backscattered electron images of the raw slimes show similar finding to that of Chen [44, 47], with clear evidence of the oxidate phase (**Figure 4.8; Table 4.8**).



## Chapter 6 Conclusions

This project examines the behavior of Te during Cu ore processing at the ASARCO mines, smelter, and refinery located near Tucson, AZ. The goals of this project was to calculate the mass balance of Te at the mine and smelter, to determine Te speciation and mineralogy in mining, smelting, and refining samples, and then to use this to identify potential waste products to target for Te extraction.

The mass balance shows that only  $2.4 \pm 0.6\%$  of the Te being purified for industrial use, when the results that  $4 \pm 1\%$  of Te mined by ASARCO reports to the Cu anode slimes are combine with a 60% extraction efficiency from the slimes. Most of the Te is lost at the mine, where  $60 \pm 30\%$  reports to the mine tailings, this step is also the largest source of uncertainty win the mass balance calculation. This may be due to Te is association with pyrite, which reports to the mine tailings. At the refinery,  $6.7 \pm 0.4\%$  of the Te is lost to waste products— $5.9 \pm 0.4\%$  is found in the gas cleaning phase and  $0.8 \pm 0.2\%$  is found in the flash furnace slag. Of all the waste products at the smelter, the gas cleaning off of the flash furnace had the highest concentration at  $158 \pm 6 \text{ mg}\cdot\text{kg}^{-1}$ . Further research will be needed to determine if the Te in this particular waste product could be extracted in the future. All of the samples at the refinery had a high concentration of Te. The raw and pressed anode slimes were  $2.4 \pm 0.1\%$  Te and  $2.7 \pm 0.1\%$  Te respectively. The increase of concentration of Te from the raw slimes to the pressed slimes indicates that much of the Te does not dissolve during the autoclaving process, but rather gets further treated in the doré furnace. The soda slag and dust filtered off this furnace were  $5,700 \pm 200 \text{ mg}\cdot\text{kg}^{-1}$  Te and  $5,800 \pm 200 \text{ mg}\cdot\text{kg}^{-1}$  respectively. Another potential source of Te is the doré furnace dust filter.

The speciation of Te changes dramatically throughout Cu ore processing. In the concentrate, Te is present as very rare telluride minerals and likely (perhaps the bulk) as nano-grains or solid solution in chalcopyrite. At the flash furnace we see that Te is 44% oxidized to  $\text{Te}^{4+}$ , which is much less than the 9% S oxidized in the same sample. In the raw slimes, Te is 67%  $\text{Te}^{2-}$  and 32%  $\text{Te}^{4+}$ . The pressed slimes do not show any more oxidization of Te with 67%  $\text{Te}^{2-}$  and 32%  $\text{Te}^{4+}$ . The doré furnace soda slag is slightly more oxidized with 52% showing as  $\text{Te}^{4+}$  and 48% as  $\text{Te}^{2-}$ . The doré furnace dust filter is even more oxidized with 76%  $\text{Te}^{4+}$  and 25%  $\text{Te}^{2-}$ .

Microprobe data found same oxidate phase as described by Chen and Dutrizac [44, 47]. These results indicate progressive oxidation of Te throughout the Cu extraction process, which is not surprising.

### *6.1 Future Directions*

Given the low extraction efficiencies of Te during Cu recovery, there are multiple processes to target for additional study to optimize Te extraction. One obvious focus are the refinery waste products due to the elevated Te concentrations. Especially important is the decopperization step in which Te is also solubilized for recovery and industrial use. Although ASARCO reports this process is 60% efficient, the pressed slimes contain high residual concentrations of Te. Other processes that could be examined for optimization at the refinery include extraction of Te from the doré furnace soda slag and possible extraction from the doré furnace dust filter, although this may be occurring within ASARCO refineries already. At the smelter, it might be possible to recover Te from the flash furnace and converter dust filters, but these only account for 5% of Te present in the original ore and Te is present at relatively low concentrations. However, some further investigation may be warranted considering the small particle size, high surface area, and partial oxidation of Te in these aerosol particles. Additional analyses of the ores, concentrates, and mine tailings are certainly needed to better define the  $60 \pm 30$  % estimate of the proportion of Te lost during the initial Cu concentration step. Once this proportion is better defined, detailed mineralogical characterization is required to determine if Te is being lost as telluride minerals or pyrite-associated Te. Little work has been performed to examine the behavior of telluride minerals during flotation conditions used in Cu extraction, and more work needs to be done to determine if a higher rate of Te retention can be obtained.

## References

1. Goldfarb, R.J., et al., *Tellurium—Economic and environmental geology, and prospects for future supply*.
2. Zemmann, J. and F. Leutwein, *Tellurium*, in *Handbook of Geochemistry*. 1978, Springer-Verlag: New York.
3. Harada, T. and Y. Takahashi, *Origin of the difference in the distribution behaviors of tellurium and selenium in a soil-water system*. *Geochimica Et Cosmochimica Acta*, 2008. **72**(5): p. 1281-1294.
4. Weeks, M.E., *The discovery of the elements. VI. Tellurium and selenium*. *Journal of Chemical Education*, 1932. **9**(3): p. 474.
5. Taylor, A., *Biochemistry of tellurium*. *Biological Trace Element Research*, 1996. **55**: p. 231-239.
6. Kyle, J.H., et al., *Review of trace toxic elements (Pb, Cd, Hg, As, Sb, Bi, Se, Te) and their deportment in gold processing. Part 1: Mineralogy, aqueous chemistry and toxicity*. *Hydrometallurgy*, 2011. **107**(3-4): p. 91-100.
7. Ojebuoboh, F., *Selenium and tellurium from copper refinery slimes and their changing applications*. *World of Metallurgy - Erzmetall*, 2008. **61**: p. 33-39.
8. George, M., *2012 minerals yearbook-selenium and tellurium*, U.S. Geological Survey, Editor. 2014.
9. George, M., *2006 minerals yearbook-selenium and tellurium*, U.S. Geological Survey, Editor. 2007.
10. George, M., *2010 minerals yearbook-selenium and tellurium*, U.S. Geological Survey, Editor. 2011.
11. Berger, L., *Semiconductor materials*. 1996: CRC press.
12. Turner, R.J., R. Borghese, and D. Zannoni, *Microbial processing of tellurium as a tool in biotechnology*. *Biotechnology advances*, 2012. **30**(5): p. 954-963.
13. Anderson, C.S., *Selenium and tellurium* U.S. Geological Survey, Editor. 2013. p. 65.1 - 65.8.

14. Zuser, A. and H. Rechberger, *Considerations of resource availability in technology development strategies: The case study of photovoltaics*. Resources Conservation and Recycling, 2011. **56**(1): p. 56-65.
15. Candelise, C., J.F. Spiers, and R.J.K. Gross, *Materials availability for thin film (TF) PV technologies development: A real concern?* Renewable & Sustainable Energy Reviews, 2011. **15**(9): p. 4972-4981.
16. Anderson, C.S., *Tellurium*, U.S. Geological Survey, Editor. 2015.
17. Kelly, T. and G. Matos, *Historical statistics for mineral and material commodities in the United States (2013 version)*, in *U.S. Geological Survey Data Series 140*. 2013.
18. Candelise, C., M. Winskel, and R. Gross, *Implications for CdTe and CIGS technologies production costs of indium and tellurium scarcity*. Progress in Photovoltaics, 2012. **20**(6): p. 816-831.
19. *First Solar Annual Report*. 2014.
20. Söderqvist, F., *Is opacity-induced minor metal market volatility a threat to promising green technologies?: A study of the tellurium market*, in *Economics*. 2013, Uppsala University.
21. Green, M., *Estimates of Te and In prices from direct mining of known ores*. Progress in Photovoltaics: Research and Applications, 2009. **17**(5): p. 347-359.
22. Houari, Y., et al., *A system dynamics model of tellurium availability for CdTe PV*. Progress in Photovoltaics: Research and Applications, 2014. **22**(1): p. 129-146.
23. Davenport, W.G., et al., *Extractive metallurgy of copper*. 4th ed. 2002, Oxford, UK: Elsevier.
24. Bartos, P., *SX-EW copper and the technology cycle*. Resources policy, 2002. **28**(3): p. 85-94.
25. Bustamante, M.L. and G. Gaustad, *The evolving copper-tellurium byproduct system: A review of changing production techniques & their implications*. Rare Metal Technology 2014, 2014: p. 11-16.
26. Edelstein, D., *Selenium and tellurium*, in *Minerals Yearbook 1989*, Bureau of Mines, Editor. 1989.

27. Jaffe, R., et al., *Energy critical elements: Securing materials for emerging technologies*. American Physical Society Panel on Public Affairs and the Materials Research Society, 2011.
28. *Critical materials strategy summary*, U.S. Department of Energy, Editor. 2010.
29. Moss, R., et al., *Critical metals in strategic energy technologies*. JRC-scientific and strategic reports, European Commission Joint Research Centre Institute for Energy and Transport, 2011.
30. Zweibel, K., *The impact of tellurium supply on cadmium telluride photovoltaics*. *Science*, 2010. **328**(5979): p. 699-701.
31. Green, M., *Rare materials for photovoltaics: Recent tellurium price fluctuations and availability from copper refining*. *Solar Energy Materials and Solar Cells*, 2013. **119**: p. 256-260.
32. Mastuyugin, S. and S. Naboichenko, *Processing of copper-electrolyte slimes: Evolution of technology*. *Russian Journal of Non-Ferrous Metals*, 2012. **53**(5): p. 367-374.
33. Chen, T. and J. Dutrizac, *Mineralogical overview of the behavior of gold in conventional copper electrorefinery anode slimes processing circuits*. *Minerals & Metallurgical Processing*, 2008. **25**(3): p. 156-164.
34. Newell, L., *Descriptive chemistry*. 1903: DC Heath & Company.
35. Marsden, J. and I. House, *The chemistry of gold extraction*. 2006: SME.
36. Christy, A., S. Mills, and A. Kampf, *A review of the structural architecture of tellurium oxycompounds*. *Mineralogical Magazine*, 2016. **80**(3): p. 415-545.
37. Knight, N., *Potential environmental risks of tellurium-rich mine tailings in a historic mining district in Delamar, Nevada*. in preparation.
38. Spry, P., et al., *The mineralogy of the Golden Sunlight gold-silver telluride deposit, Whitehall, Montana, U.S.A*. *Mineralogy and Petrology*, 1997. **59**(3-4): p. 143-164.
39. Chizhikov, D. and V. Schastlivyi, *Tellurium and tellurides*. 1966. NAUKA, MOSCOW, 279 P, 1967.
40. Brookins, D., *Eh-pH diagrams for geochemistry*. 1988.



41. Yano, R., *Trace element distribution in chalcopyrite-bearing porphyry and skarn deposits*. 2012, University of Nevada, Reno.
42. Reich, M., et al., *Pyrite as a record of hydrothermal fluid evolution in a porphyry copper system: A SIMS/EMPA trace element study*. *Geochimica et Cosmochimica Acta*, 2013. **104**: p. 42-62.
43. Bulatovic, S., *Flotation behaviour of gold during processing of porphyry copper-gold ores and refractory gold-bearing sulphides*. *Minerals Engineering*, 1997. **10**(9): p. 895-908.
44. Chen, T. and J. Dutrizac. *The deportment of selenium and tellurium during the electrorefining of copper*. 2000. Society for Mining, Metallurgy, and Exploration.
45. Moats, M., et al. *Electrolytic copper refining—2007 world tankhouse operating data*. in *Copper-Cobre 2007 International Conference*. 2007.
46. Chen, T. and J. Dutrizac, *Practical mineralogical techniques for the characterization of hydrometallurgical products*. *Process Mineralogy IX: Applications to Mineral Beneficiation, Metallurgy, Gold, Diamonds, Ceramics, Environment and Health*, 1989: p. 289-309.
47. Chen, T. and J. Dutrizac, *Mineralogical characterization of anode slimes: Part 10. Tellurium in raw anode slimes*. *Canadian Metallurgical Quarterly*, 1996. **35**(4): p. 337-351.
48. Robles-Vega, A., V. Sanchez-Corrales, and F. Castillon-Barraza, *An improved hydrometallurgical route for tellurium production*. *Minerals & Metallurgical Processing*, 2009. **26**(3): p. 169-173.
49. Hoffmann, J.E., *Recovering selenium and tellurium from copper refinery slime*. *JOM*, 1989. **41**(7): p. 33-35.
50. Hoffmann, J.E., *Processing slimes: The base case and opportunities for improvement*. *JOM*, 1990. **42**(8): p. 38-38.
51. Ekholm, J., *ASACRO Mission Complex fact sheet*. 2008.
52. Williamson, R., *Geology of the mineral hill area, Mission Mine, Pima County, Arizona*. 1993.
53. *Mission Pit*. Available from: <http://www.mindat.org/loc-32002.html>.

54. *Ray Mine*. Available from: <http://www.mindat.org/loc-3377.html>.
55. Hayes, S., et al., *Surficial weathering of iron sulfide mine tailings under semi-arid climate*. *Geochimica et cosmochimica acta*, 2014. **141**: p. 240-257.
56. Longerich, H., et al., *Inductively coupled plasma-mass spectrometric analysis of geological samples - A critical evaluation based on case studies*. *Chemical Geology*, 1990. **83**(1-2): p. 105-118.
57. Skoog, D., F. Holler, and S. Crouch, *Principles of Instrumental Analysis*. 6 ed. 2007, California, United States: Thomson Higher Education.
58. Harris, D., *Quantitative Chemical Analysis*. 2010: W. H. Freeman.
59. Ellison, S. and M. Thompson, *Standard additions: Myth and reality*. *Analyst*, 2008. **133**(8): p. 992-997.
60. Cotta, A. and K.ENZWEILER, *Classical and new procedures of whole rock dissolution for trace element determination by ICP-MS*. *Geostandards and Geoanalytical Research*, 2011. **36**(1): p. 27-50.
61. Meisel, T., et al., *Determination of rare earth elements, Y, Th, Zr, Hf, Nb and Ta in geological reference materials G-2, G-3, SCo-1 and WGB-1 by sodium peroxide sintering and inductively coupled plasma-mass spectrometry*. *Geostandards Newsletter-the Journal of Geostandards and Geoanalysis*, 2002. **26**(1): p. 53-61.
62. Potts, P., *Handbook of rock analysis*. 2003: Viridian.
63. Jenkins, R., *Quantitative x-ray spectrometry*. 1995: CRC Press.
64. Calvin, S., *XAFS for Everyone*. 2013, New York: CRC Press.
65. Brown, G. and N. Sturchio, *An overview of synchrotron radiation applications to low temperature geochemistry and environmental science*. *Applications of Synchrotron Radiation in Low-Temperature Geochemistry and Environmental Science*, ed. J. Rosso and P. Ribbe. Vol. 49. 2002, Washington, D.C.: The Mineralogical Society of America.
66. Myneni, S., *X-ray and vibrational spectroscopy of sulfate in earth minerals*. *Sulfate Minerals-Crystallography, Geochemistry, and Environmental Significance*, ed. P. Ribbe. Vol. 40. 2000, Washington, D.C.: The Mineralogical Society of America.
67. Newville, M., *Periodic table of x-ray absorption and emission energies*. 2013.

68. Webb, S., *Sixpack: A graphical user interface for XAS analysis using IFEFFIT* *Physica Scripta*, 2005: p. 1011-1014.
69. Sutton, S., *Microfluorescence and microtomography analyses of heterogeneous earth and environmental materials*, in *Applications of Synchrotron Radiation in Low-Temperature Geochemical and Environmental Science*, J. Rosso and P. Ribbe, Editors. 2002, The Mineralogical Society of America: Washington, D.C. p. 429-478.
70. Thompson, A., et al., *X-ray data booklet*. 3rd ed. 2009, Berkeley, CA: Lawrence Berkeley National Laboratory.
71. Yang, Y., *The effect of microorganisms on the surface properties of chalcopyrite*, in *School of Chemical & Physical Sciences*. 2014, Flinders University.
72. Webb, S., *Sam's Microprobe Analysis Kit*. 2010:  
[http://home.comcast.net/~sam\\_webb/smak.html](http://home.comcast.net/~sam_webb/smak.html).
73. Rodushkin, I., E. Engström, and D. Baxter, *Sources of contamination and remedial strategies in the multi-elemental trace analysis laboratory*. *Analytical and Bioanalytical Chemistry*, 2009. **396**(1): p. 365-377.
74. Foster, A.L., et al., *Quantitative arsenic speciation in mine tailings using x-ray absorption spectroscopy*. *American Mineralogist*, 1998. **83**(5-6): p. 553-568.
75. Coleman, R. and M. Delevaux, *Occurrence of selenium in sulfides from some sedimentary rocks of the western United States*. *Economic Geology*, 1957. **52**(5): p. 499-527.